

Fall 2013

Energy resolution analysis of a domestic neutron imager

Marissa Louise Rousseau
University of New Hampshire, Durham

Follow this and additional works at: <https://scholars.unh.edu/thesis>

Recommended Citation

Rousseau, Marissa Louise, "Energy resolution analysis of a domestic neutron imager" (2013). *Master's Theses and Capstones*. 805.
<https://scholars.unh.edu/thesis/805>

This Thesis is brought to you for free and open access by the Student Scholarship at University of New Hampshire Scholars' Repository. It has been accepted for inclusion in Master's Theses and Capstones by an authorized administrator of University of New Hampshire Scholars' Repository. For more information, please contact nicole.hentz@unh.edu.

ENERGY RESOLUTION ANALYSIS OF A DOMESTIC NEUTRON IMAGER

BY

MARISSA LOUISE ROUSSEAU

B.S., University of New Hampshire, 2011

THESIS

Submitted to the University of New Hampshire
in Partial Fulfillment of
the Requirements for the Degree of

Master of Science

in

Physics

September, 2013

UMI Number: 1524304

All rights reserved

INFORMATION TO ALL USERS

The quality of this reproduction is dependent upon the quality of the copy submitted.

In the unlikely event that the author did not send a complete manuscript and there are missing pages, these will be noted. Also, if material had to be removed, a note will indicate the deletion.



UMI 1524304

Published by ProQuest LLC 2013. Copyright in the Dissertation held by the Author.

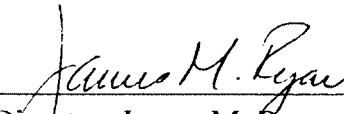
Microform Edition © ProQuest LLC.

All rights reserved. This work is protected against unauthorized copying under Title 17, United States Code.

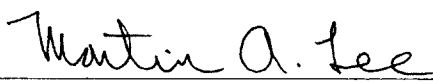


ProQuest LLC
789 East Eisenhower Parkway
P.O. Box 1346
Ann Arbor, MI 48106-1346

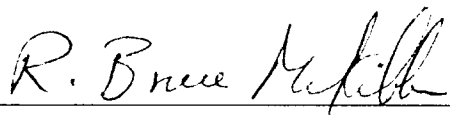
This thesis has been examined and approved.



Thesis Director, James M. Ryan,
Professor of Earth, Oceans, and Space and Physics



Martin A. Lee,
Professor of Earth, Oceans, and Space and Physics



R. Bruce McKibben,
Affiliate Professor of Earth, Oceans, and Space and Physics



Date

ACKNOWLEDGEMENTS

This thesis would not have been possible without the guidance of my committee members or the encouragement of my friends and family.

I would like to thank my advisor, Dr. James Ryan, for giving me the opportunity to work with an outstanding team of faculty and students on an incredibly fascinating instrument. I would also like to express my sincerest gratitude for his endless source of knowledge, support, and patience.

Finally, I would like to thank my parents and brother for believing in me and for helping me to keep at my research, even during the most anxious of moments.

TABLE OF CONTENTS

ACKNOWLEDGEMENTS.....	iii
LIST OF FIGURES	vi
ABSTRACT.....	x
1. INTRODUCTION	1
2. DEVELOPMENT OF A NEUTRON SPECTROMETER.....	3
2.1. The Neutron Spectroscope (NSPECT)	5
2.2. Time-of-Flight Calibration, Characterization, and Correction	8
2.3. Time-of-Flight Logic and Hardware.....	9
2.4. Walk Correction.....	11
2.5. Calibrating the Time-of-Flight Circuit.....	16
2.6. Cell Electronics Offsets	17
2.7. Fully Corrected Time-of-Flight Analysis	20
2.8. Neutron Detection.....	23
2.9. Final Remarks	25
2.9.1. Checking NSPECT Hardware.....	26
2.9.2. Checking Walk Correction	27
2.9.3. Checking Calibration to Nanoseconds.....	28
2.9.4. Checking Electronics Offsets.....	29
3. AN INSTRUMENT FOR THE ASSAY OF NUCLEAR REACTOR FUEL.....	32
3.1. A Summary of Nuclear Power Reactor Theory	33
3.1.1. Nuclear Fission Physics	33

3.1.2. Fission Power Reactors.....	35
3.1.3. Neutron Moderation and Reactor Criticality	37
3.1.4. Power Reactor Design.....	38
3.1.5. Neutron Poisons	40
3.1.6. Waste Management.....	41
3.2. Applications for Proposed Detector.....	42
3.3. Optimization for Detecting (α , n) Neutrons	46
3.3.1. Analytical Model of Neutron Detection Physics	46
3.3.2. Procedure for Optimization.....	51
3.3.3. Analysis Limitations	52
3.4. Comparing Design to NSPECT	54
3.5. Final Remarks	56
4. CONCLUSION.....	57
LIST OF REFERENCES	58
APPENDIX.....	59
A.1. Data Characterization.....	62
A.1.1. Angular Resolution Measure	63
A.1.2. Compton Scattering.....	64
A.2. Analysis & Results.....	66
A.3. Discussion	72
A.4. Final Remarks	74

LIST OF FIGURES

- Figure 2.1. Photo of NSPECT. The left-most layer is D1, the middle layer is D2, and the right-most layer is D3. The scintillators are one inch right circular cylinders located in the front cap of each cell..... 5
- Figure 2.2. Constructing a neutron-source image. The origin is defined at the center of D2. Each ellipse on the image represents a detected neutron. A red star indicates the source location. 6
- Figure 2.3. Image analysis of a ^{252}Cf source placed one meter off-axis. (a) A dark circle is drawn over the image at the source location. The size of the circle represents the image resolution. (b) Selecting data inside the circle produces a clean energy spectrum of the source. 7
- Figure 2.4. Illustration of a ToF spectrum (From Knoll¹). The ToF resolution is reported as the full-width-at-half-maximum (FWHM) of the peak. 8
- Figure 2.5. Each cell contains a solid scintillator, a PMT, and a preamplifier. 9
- Figure 2.6. The CFD process (From Knoll¹). The incoming voltage pulse (a) is split into two identical voltage pulses: one is multiplied by the desired percentage f (b) while the other is inverted and delayed (c). The two pulses are summed (d) and a fast logic signal is generated when the voltage crosses zero. 10
- Figure 2.7. Walk from a CFD (From Leo²). Inputs with different pulse shapes (solid vs. dashed lines) create fluctuations in the timing of fast logic signal generation as a function of pulse-height. 11
- Figure 2.8. Walk from a level discriminator (From Knoll¹). A fast logic pulse is generated when the incoming voltage pulse exceeds a specified value. This method is very sensitive to the input pulse shape. 12
- Figure 2.9. The ToF correction and calibration setup. A double-photon γ -ray source is placed directly between the central cells in D1 and D2. 12

Figure 2.10. A density plot of the ^{60}Co energy spectrum measured with D1_{C13} and D2_{C13}. The blue (D1 fixed) and red (D2 fixed) boxes demonstrate how data were selected for the ToF walk analysis..... 14

Figure 2.11. The fit results for the mean ToF versus the weighted average pulse-height (a). These data were translated to create the walk correction (b). Walk shifts the ToF by up to 70 channels in each layer. 15

Figure 2.12. The ADC channel assigned by the TAC corresponds linearly to the time between two coincident events plus any delays introduced to the circuit. Calibration of the NSPECT ToF circuit resulted in a scaling factor of 14.8 channels per nanosecond..... 16

Figure 2.13. The bold orange arrow demonstrates how the path length to a cell in D2 differs from the path length to the central D1 cell. The ToF is normalized to account for this. 18

Figure 2.14. Scatter plot (a) and histogram (b) of the difference in γ -ray travel time (ΔT) due to path lengths from the calibration source to each cell in a detector plane. Normalization is achieved by subtracting ΔT from the ToF for each cell..... 19

Figure 2.15. Cell address numbering is the same for all layers. In reference to the NSPECT coordinate system, the z-axis points into the page and the origin of the x-y plane is located at cell 13. 19

Figure 2.16. Scatter plot (a) and histogram (b) of the mean ToF for all forty-nine cell combinations. These values represent the electronics offsets for their respective cells in D1 and D2. 20

Figure 2.17. Progression of ToF corrections: (a) The raw ToF data obtained from NSPECT, (b) the walk corrected ToF, and (c) the fully calibrated and corrected ToF. 21

Figure 2.18. The fully corrected ToF and the FWHM as a function of the energy deposited in D1 and D2..... 22

Figure 3.1. A model of the proposed neutron detector. A neutron with incident kinetic energy E_n deposits energy E_I as it scatters in D1. The scattered neutron travels with a kinetic energy E_T to D2. 32

Figure 3.2. Illustration of how (α, n) reactions in UO_2 fuel might modify the fission spectrum. The solid red line is the fission spectrum. The dashed green line is what might be revealed if the fission spectrum was removed. 45

Figure 3.3. An illustration for approximating the solid angle of D2 in the laboratory frame. Neutrons are assumed to scatter at the center of D1. The radius R of each cell is 2.54 cm. 50

Figure 3.4. Equations (3.8) and (3.16) are plotted in (a) and (b), respectively, as a function of L and Θ . The dashed green line marks a neutron energy resolution of 0.2 MeV FWHM. The solid white line is drawn at the D1/D2 cell separation in NSPECT..... 52

Figure 3.5. Co-60 energy spectrum and energy resolution measured with (a) D1 and (b) D2 cells in the two-cell setup..... 54

Figure 3.6. Co-60 energy spectrum measured with (a) D1 and (b) D2 layers in NSPECT. The energy resolution function for each detection layer has yet to be determined. . 55

Figure A.1. Density plot of ^{60}Co energy spectra measured by the D1 and D2 detector planes. The ^{60}Co data presented are the same calibration data used in Chapter 2.... 59

Figure A.2. Measurements of (a) the ARM, (b) the ToF, (c) energy in D1, and (c) energy in D2 from a ^{137}Cs source placed on-axis and 2 m in front of NSPECT. (continued) 60

Figure A.3. Compton scatter results for ^{137}Cs 65

Figure A.4. Isolating the forward scatter peak of the ^{137}Cs data ($1.25 \text{ ns} \leq \text{ToF} \leq 1.86 \text{ ns}$). Measurements of (a) D1 energy and (b) D2 Energy. (continued) 66

Figure A.5. Isolating the backward scatter peak of the ^{137}Cs data ($-1.86 \text{ ns} \leq \text{ToF} \leq -1.25 \text{ ns}$). Measurements of (a) D1 energy, (b) D2 energy, (c) the net energy in D1 and D2, and (d) the ARM distribution. (continued) 68

Figure A.6. Restricting the forward scatter peak data to $\pm 5^\circ$ ARM measurements. Histograms of (a) D1 energy, (b) D2 energy, and (c) the net energy in D1 and D2. (d) A density plot of the D1 and D2 energies. 70

Figure A.7. The same ^{137}Cs data with measurements from the D2 and D3 detector planes. Measurements of (a) D2 energy, (b) D3 energy, (c) the net energy in D2 and D3, and (d) the ARM distribution. (continued) 71

Figure A.8. Cs-137 D2-D3 coincidence data restricted to $\pm 5^\circ$ ARM measurements. Histograms of (a) D2 energy, (b) D3 energy, and (c) the net energy in D2 and D3. (d) A density plot of the D2 and D3 energies 73

ABSTRACT

ENERGY RESOLUTION ANALYSIS OF A DOMESTIC NEUTRON IMAGER

by

Marissa Louise Rousseau

University of New Hampshire, September, 2013

The calibration and correction of the Neutron Spectroscopy (NSPECT) time-of-flight (ToF) system are presented. This instrument is a double-scatter telescope designed to detect neutrons and gamma rays for the identification and location of radioactive materials. The ToF resolution is 0.72 ns FWHM. Results are reported for the ToF characterization using data obtained in the laboratory. An anomalous feature in the gamma-ray energy spectra measured with NSPECT neutron detectors is examined.

A design based on NSPECT is proposed for the assay of spent nuclear fuel, where portability is increased in exchange for source location capabilities. The proposed modular device is modifiable for numerous safety applications at participating facilities in the nuclear fuel cycle. Optimization of the instrument to characterize alpha-neutron reactions in irradiated fuel is discussed. A delicate balance between energy resolution and detector efficiency is required. Results from laboratory testing are reported and compared to NSPECT measurements.

1. INTRODUCTION

The Neutron Spectroscope (NSPECT) is a prototype instrument developed at the University of New Hampshire with funding from the Defense Threat Reduction Agency (DTRA). It has the ability to detect, identify, and locate neutron and γ -ray sources. This makes NSPECT useful in numerous security or safety related scenarios. NSPECT is also portable, and its design can be easily adapted to facilitate operation and optimize performance in specific scenarios.

One possible application for a simplified version of NSPECT is at a nuclear power reactor. Nuclear power reactors convert the heat from radioactive fuel into mechanical energy by spinning a turbine. This is analogous to the combustion of fossil fuels, which also generates mechanical energy from heat, though not necessarily by spinning a turbine.

Most nuclear reactor fuel is composed of a fissionable material – typically uranium – that is mixed as a powder with oxides and binding materials, compressed and heated into pellets, and then stacked in metal tubes called fuel rods. Like any other power source, nuclear reactors must eventually be refueled. Unlike fossil-fuels however, reactor fuel loses its ability to sustain the desired energy output before it is entirely consumed. What remains in the fuel rods is referred to as spent fuel. Refueling of a nuclear reactor requires replacing the spent fuel, which still emits significant amounts of radiation, with new fuel rods. The spent fuel rods will continue to produce radiation long after they are removed from the reactor. Consequently, they are placed in shielded containers designed to store the fuel indefinitely.

The main advantage of developing a device based on the NSPECT instrument for use at a nuclear power reactor is its ability to assay spent reactor fuel at safe distances. The fuel rods need not be removed from storage, or perhaps even from the reactor, in order to perform measurements. This reduces the risk of exposure, and can be done without destroying the spent fuel rods, which is often required for current assay methods. Such a device would have limited source location capabilities as a result of its simplified design. It could also potentially be integrated into systems or procedures currently in place to monitor for, and respond to, contamination resulting from an equipment malfunction or operational error.

Data obtained from the assay of spent reactor fuel could provide information on their radioactive content. This is important for many reasons. First, it can be used to determine when a reactor has cooled sufficiently so it can be safely opened for refueling and also monitor the refueling process. It can provide insight into the types of neutron poisons that form during operation and the storage methods used for spent fuel rods. Finally, if a reactor is forced to shut down abruptly, the activity of the fuel will be known. In the event of an accident this information may be critical for evaluating the impact of damaged systems, monitoring for leaks, locating where radioactive material is escaping the reactor, and identifying the radioactive material that is released.

The design of an instrument for analyzing spent reactor fuel is proposed in Chapter 3. It is a logical extension of the NSPECT design that is capable of high-resolution neutron spectroscopy to determine the fuel composition. The calibration and characterization of a major feature that enables NSPECT to perform neutron spectroscopy is discussed in Chapter 2.

2. DEVELOPMENT OF A NEUTRON SPECTROMETER

Radiation spectroscopy is used to characterize materials based on the unique energy signatures of the radiation they emit. Spectrometers are often designed to detect neutrons or γ rays because these particles can travel considerable distances through matter without interacting. This also makes them difficult to detect, but not impossible.

Radiation detection results most commonly from an interaction between charged particles and electrons in the detector material. Neutrons, because they have no net charge, must therefore trigger a reaction that generates charged particles to be detected. As a result, measuring incident neutron energies is not easily achieved with a single detector because it does not directly detect the neutrons.

In general, the materials used in neutron detectors must have a high probability for neutron-induced reactions that produce charged particles. We focus on the detection of fast neutrons with energies between 0.5 MeV and 15 MeV. Fast neutron detectors typically contain light nuclei to take advantage of their large cross sections for neutron elastic scattering. Other neutron detectors exist that rely on a variety of neutron interactions, but they will not be discussed in this thesis.

Hydrogen-dense scintillators are a popular choice for detecting fast neutrons. The incident neutrons scatter elastically off hydrogen nuclei in the detector to yield energetic recoil protons. A neutron can transfer up to 100% of its kinetic energy to the hydrogen nucleus in this manner. The recoil protons will either excite or ionize atoms in the scintillator causing it to fluoresce. The amount of light produced by the scintillator is a measure of the energy lost by the incident neutron.

Neutrons are not affected by external forces as they travel through a medium unless they come in direct contact with nuclei. Fast neutron energies are also within a range where crystalline, magnetic, and relativistic effects are negligible [1]. This means that, between interactions, fast neutrons travel at constant, subluminal velocities with non-relativistic kinetic energies.

A common approach to measuring incident neutron energies is to use a double-scatter telescope consisting of two neutron detectors. When a neutron scatters in the first detector, it measures the recoil proton energy and sends a signal to start a timer. The timer is stopped if the neutron scatters in the second detector. The time elapsed between the start and stop signals is called the *time-of-flight*, and it is inversely proportional to the neutron velocity as it travels between the two detectors.

Double-scatter telescopes use coincidence counting to place an upper limit on the time-of-flight (ToF). This ensures that the same neutron is responsible for triggering both detectors. The velocity of a neutron after it scatters in the first detector can be calculated by dividing the distance between the detectors by the ToF. With its velocity known, the kinetic energy of the neutron is easily calculated. The incident energy of a detected neutron is thus the sum of the energy it deposited in the first detector and its kinetic energy after it scatters, assuming no additional interactions occurred as the neutron traveled to the second detector.

2.1. *The Neutron Spectroscope (NSPECT)*

NSPECT is a double-scatter telescope for the detection of both neutrons and γ rays. As shown in Figure 2.1, it contains three layers, or detector planes, of scintillation detectors. There are twenty-five scintillation detectors (cells) in each detector plane. The cells in the first detector plane (D1) and the second detector plane (D2) contain, respectively, plastic and stilbene scintillators. Only D1 and D2 are used to detect neutrons. The third detection plane is strictly for γ -ray spectroscopy and does not contribute to this analysis.

The NSPECT instrument was designed to locate the source of radiation and to measure neutron and γ -ray spectra. The process for locating a neutron source, illustrated in Figure 2.2, is as follows: The scatter angle is calculated using the energy measured in D1 and the kinetic energy of the scattered neutron. This angle defines a cone with vertex

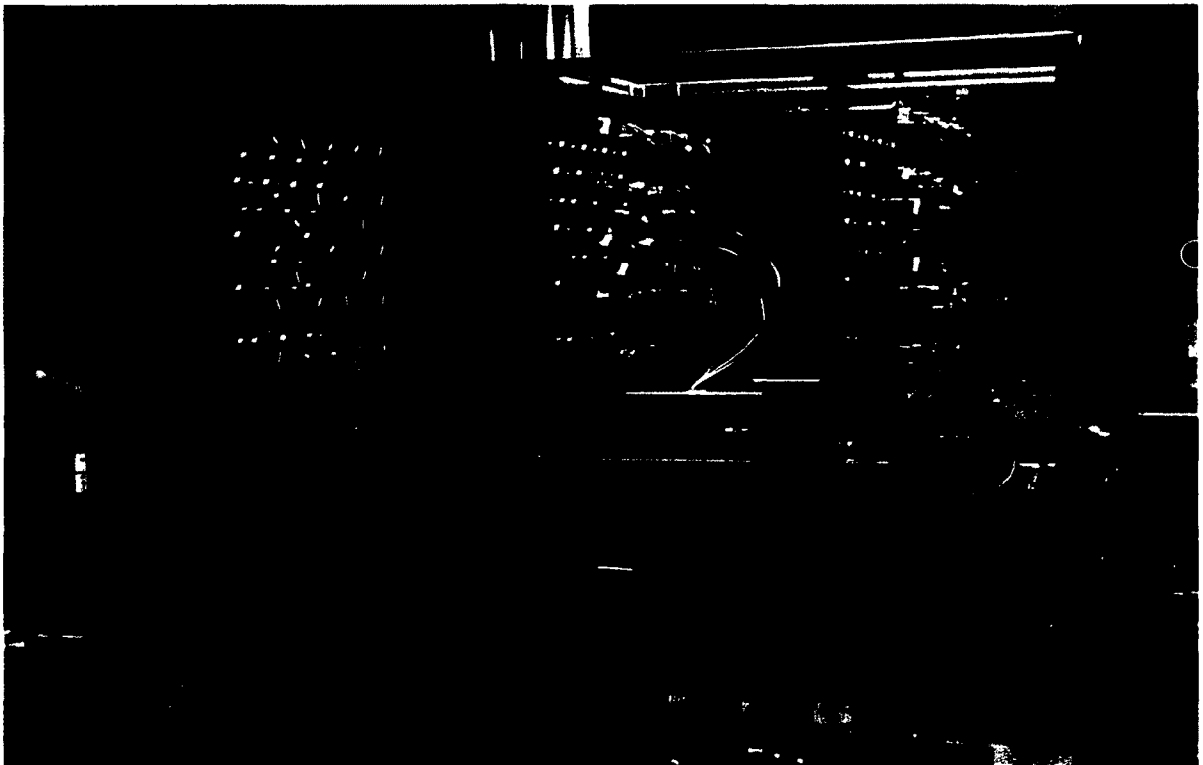


Figure 2.1. Photo of NSPECT. The left-most layer is D1, the middle layer is D2, and the right-most layer is D3. The scintillators are one inch right circular cylinders located in the front cap of each cell.

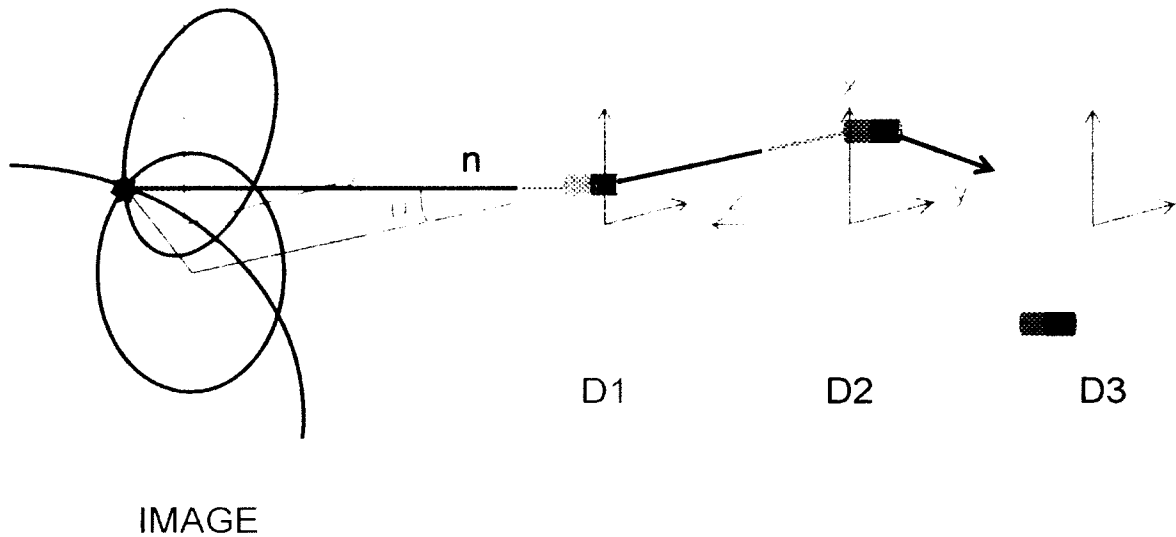


Figure 2.2. Constructing a neutron-source image. The origin is defined at the center of D2. Each ellipse on the image represents a detected neutron. A red star indicates the source location.

at the triggered cell in D1 and axis parallel to the scattered neutron path. The cone can be projected onto a plane (x, y) located at the source. The distance (z) from the plane to NSPECT, which may need to be assumed, is required to do this. The projection results in an ellipse of possible source locations drawn on the plane. Each detected neutron produces a new ellipse. The ellipses overlap to produce an “image” of the neutron source on the plane. Adjusting the z coordinate has the effect of “focusing” the image. The x and y coordinates of the image are determined by numerically locating the region with the highest density of ellipse overlap.

An example of the image produced with this process is shown in Figure 2.3. The analysis was performed using data acquired in the laboratory with a ^{252}Cf source. The source was placed one meter off-axis ($+y$ direction) and two meters in front of NSPECT. A circle has been drawn on top of the image at the known position of the source. The size of this circle is based on the imaging resolution. Data were selected within the circle to

produce a histogram of incident neutron energies. This selection minimizes the number of events caused by background and random coincidence.

The scintillators in D1 and D2 are sensitive to both neutrons and γ rays, but only the neutrons were used to construct the image in Figure 2.3. This is because D1 and D2 are unable to capture the full incident γ -ray energies as they interact in the scintillators via Compton scattering. Without the complete incident γ -ray energies, scatter angles calculated using the Compton energy equation will produce a distorted image.

Separation of neutron events from γ -ray events is achieved by means of the ToF measurements and the pulse-shape-discrimination (PSD) properties in the D2 scintillators. Section 2.8 provides a brief discussion of the PSD measurement and the routine currently implemented in the NSPECT software for distinguishing between neutrons and γ rays.

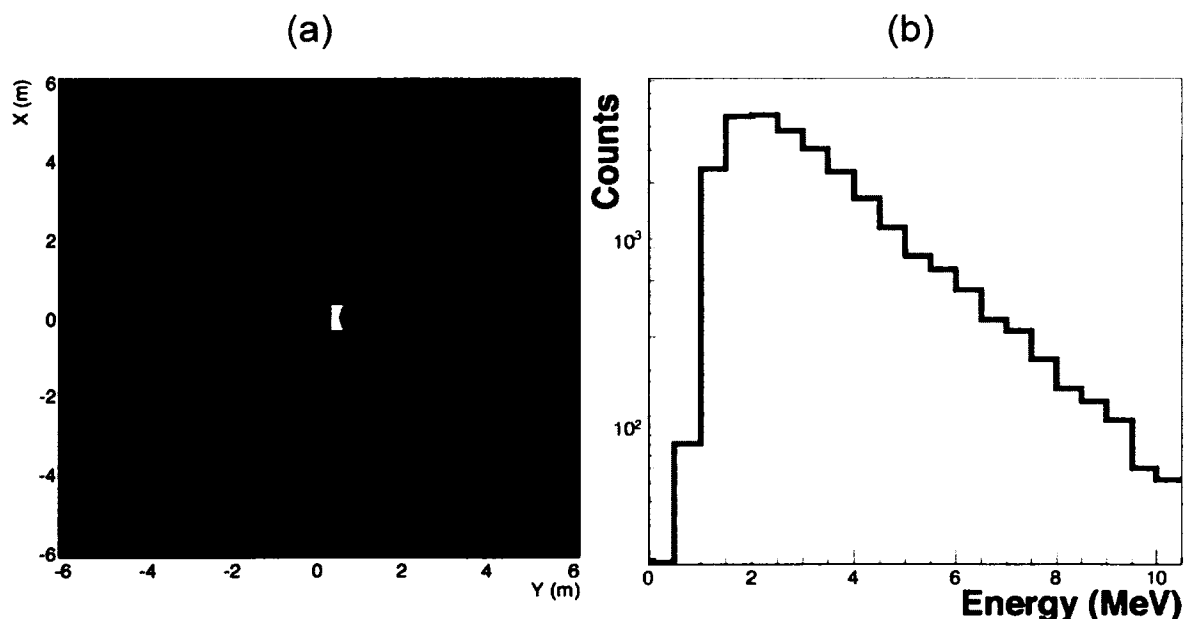


Figure 2.3. Image analysis of a ^{252}Cf source placed one meter off-axis. (a) A dark circle is drawn over the image at the source location. The size of the circle represents the image resolution. (b) Selecting data inside the circle produces a clean energy spectrum of the source.

2.2. Time-of-Flight Calibration, Characterization, and Correction

The time-of-flight (ToF) is a measure of the time elapsed between cell triggers of *coincident events* (the same particle is detected once in each layer). As discussed earlier in this chapter, the neutrons detected by NSPECT have energies low enough to ignore relativistic effects during analysis. The ToF therefore relates directly to the neutron velocity, and may be used to calculate its kinetic energy.

The ToF spectrum for a beam of monoenergetic, identical, particles should ideally be a delta function. In reality, the ToF measurement process is not precise enough to result in such a spectrum. Various random and systematic uncertainties broaden the ToF to a Gaussian-like peak similar to the one shown in Figure 2.4. The accuracy with which an instrument measures any quantity that follows Gaussian statistics is defined as its *resolution*, and it will be smaller for measurements that are more precise.

There are many factors that affect the ToF resolution of NSPECT. The systematic uncertainties are often controllable, and may therefore be removed or reduced. These include (1) delays that are intentionally introduced into the ToF electronics to facilitate measurement, (2) the deviation of the ToF as a function of the detected particle energy,

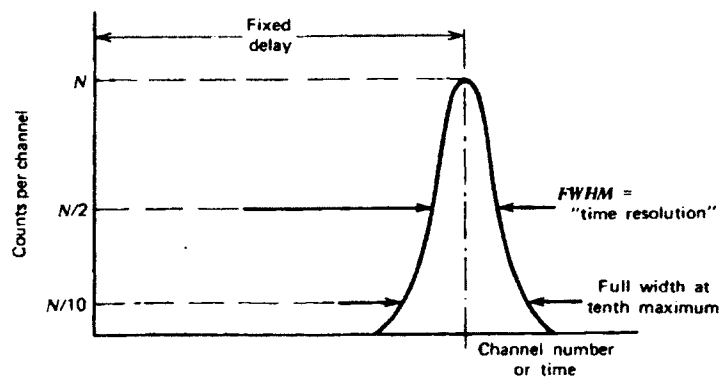


Figure 2.4. Illustration of a ToF spectrum (From Knoll¹). The ToF resolution is reported as the full-width-at-half-maximum (FWHM) of the peak.

(3) the channel number assigned to a ToF measurement by an analog-to-digital converter (ADC), and (4) the uniqueness of the electronics in each cell.

The process of correcting systematic uncertainties is described in Sections 2.4 through 2.6. These corrections improve the ToF resolution; however, random uncertainties will remain that cannot be removed. These include (1) the inability to detect the exact location where a particle interacted inside a cell and (2) minute instabilities in signals from the cell electronics.

2.3. Time-of-Flight Logic and Hardware

Each cell in NSPECT contains a scintillator, a photomultiplier tube (PMT), and a preamplifier (Figure 2.5). Photons are emitted as a result of an incoming particle interacting in the scintillator material. In response to the scintillator light output, the PMT generates a cascade of electrons to produce a current pulse. This current pulse is converted to a voltage pulse by the preamplifier. The *pulse-height* (voltage pulse amplitude) is directly proportional to the energy deposited into the cell by the particle. Additionally, in D2, the pulse shape depends on the type of particle detected.

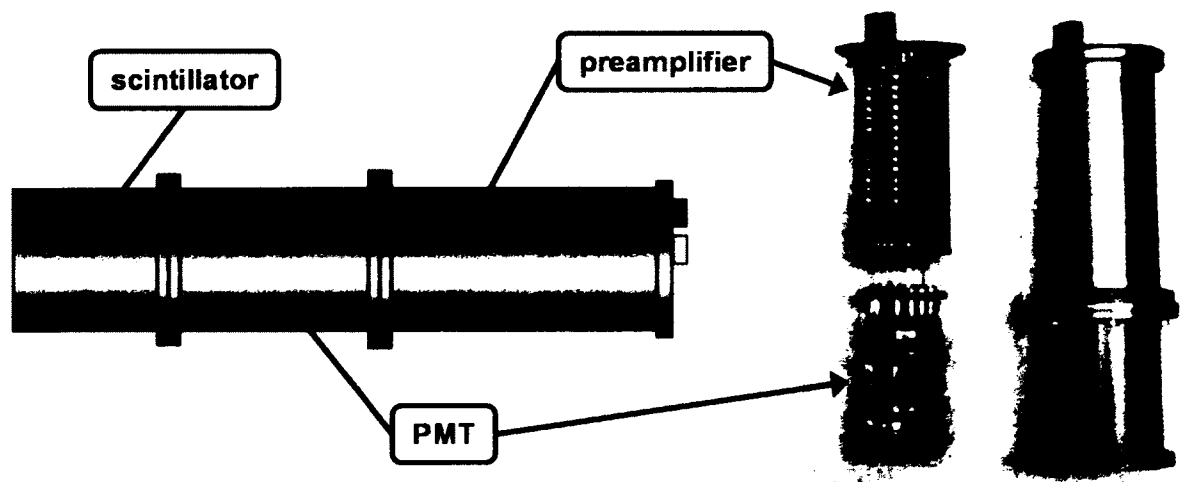


Figure 2.5. Each cell contains a solid scintillator, a PMT, and a preamplifier.

Voltage pulses are split and fed into processing electronics for applying coincidence criteria; identifying the triggered cell; and performing ToF, PSD, and pulse-height measurements. An event is discarded if multiple cells are triggered in a single layer. This is important because the ToF signal is summed over all twenty-five cells in a detector plane before it is fed to the ToF processing electronics. Multiple scatters in one layer will also result in unphysical scatter angles, which will affect the source image.

The ToF processing electronics contain a constant fraction discriminator (CFD) that takes the summed analog signal from a detector plane and generates a fast logic pulse. A detailed explanation of the CFD is provided in Figure 2.6. The fast logic pulses

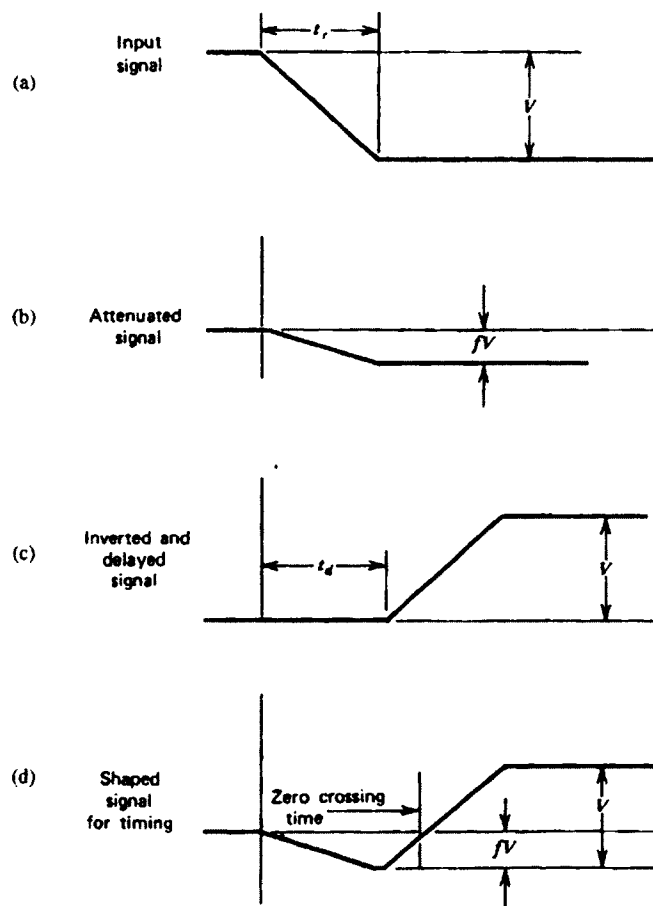


Figure 2.6. The CFD process (From Knoll¹). The incoming voltage pulse (a) is split into two identical voltage pulses: one is multiplied by the desired percentage f (b) while the other is inverted and delayed (c). The two pulses are summed (d) and a fast logic signal is generated when the voltage crosses zero.

from D1 and D2 function, respectively, as start and stop signals for a time-to-amplitude converter (TAC). These pulses are also used to determine if an event meets the 50-ns coincidence requirement. If coincidence is not satisfied the event is discarded.

To ensure that the start signal always arrives first and that the TAC has sufficient processing time, a 50-ns delay is added to the stop signal. The start signal triggers a constant current source in the TAC that charges a capacitor. The capacitor continues charging until the TAC receives a stop signal. The voltage across the capacitor as it charges corresponds to the time elapsed between cell triggers in D1 and D2, plus the 50-ns delay. The ADC assigns a channel number to this voltage that is later written to an ASCII file along with other measurements gathered from the detected event.

2.4. Walk Correction

The shape of the voltage pulse from the triggered cell will depend somewhat on its pulse-height and may delay signals from the CFD. This will cause deviations in the ToF as a function of pulse-height – a concept referred to as *walk*. ToF walk from a CFD and a level discriminator are shown in Figure 2.7 and Figure 2.8 respectively. These figures demonstrate how first order corrections for walk will be smaller for a CFD than for a level discriminator.

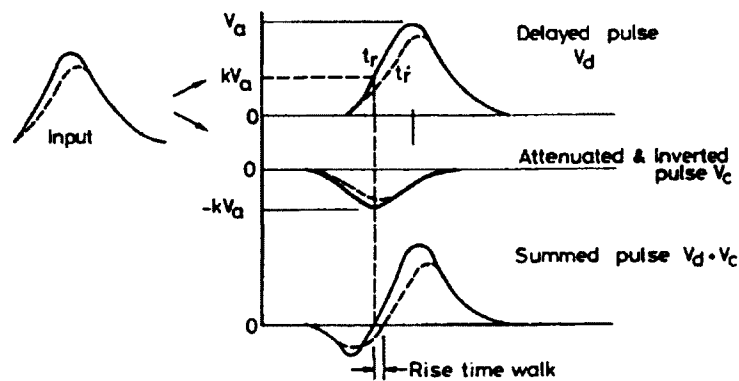


Figure 2.7. Walk from a CFD (From Leo²). Inputs with different pulse shapes (solid vs. dashed lines) create fluctuations in the timing of fast logic signal generation as a function of pulse-height.

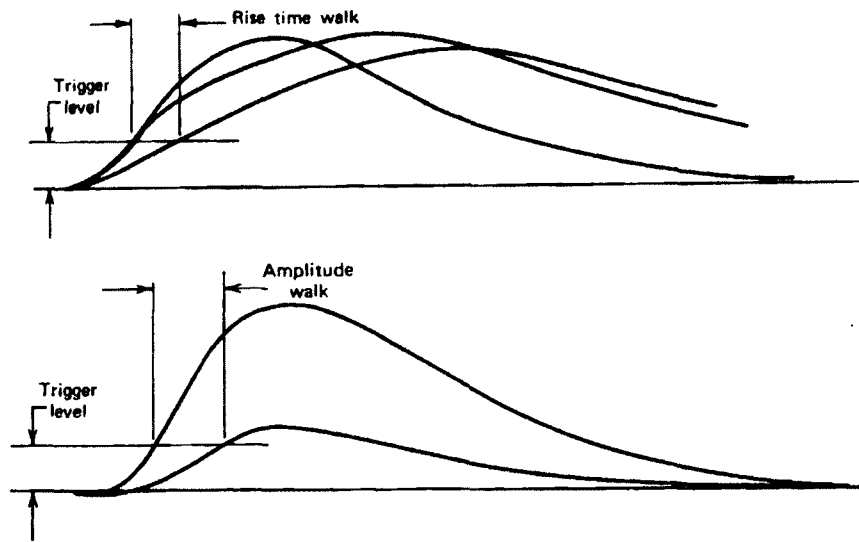


Figure 2.8. Walk from a level discriminator (From Knoll¹). A fast logic pulse is generated when the incoming voltage pulse exceeds a specified value. This method is very sensitive to the input pulse shape.

To correct for walk, the relationship between ToF and pulse-height must be determined. This is done by placing a double-photon γ -ray source on-axis and directly between D1 and D2 as shown in Figure 2.9. The cells located in the center of each detector plane are closest to the source, and are therefore most likely to have the highest count rates. These cells (named D1_{C13} and D2_{C13}) should measure an average ToF of 0 ns because γ rays from the source will be detected quasi-simultaneously.

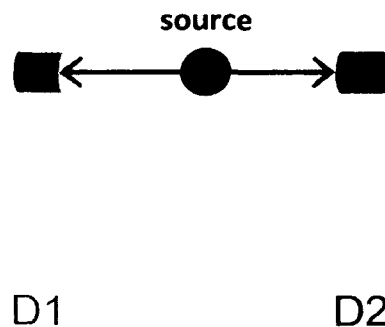


Figure 2.9. The ToF correction and calibration setup. A double-photon γ -ray source is placed directly between the central cells in D1 and D2.

The ToF is summed over all cells in a detector plane, which means walk should be independent of the cells used to measure it. This will not be true if the ToF data is evaluated for walk after the pulse-height is calibrated from the assigned ADC channel to energy in kiloelectronvolts (keV). Each cell is calibrated independently because they generate voltage pulses with slightly different amplitudes for the same deposited energy. In other words, the same pulse-height from any cell will not necessarily correspond to the same energy; however, it will create the same amount of walk. The effect of individual cells on the ToF will be addressed in Section 2.6.

Data were taken using a ^{60}Co source, which emits two quasi-simultaneous γ rays. These γ rays are uncorrelated, which means all angles of emission are equally probable. The ToF spectrum for a γ -ray source in this configuration, using only events between D1_{C13} and D2_{C13}, would ideally be a delta function at 0 ns. Walk broadens the ToF spectrum because each detected γ ray deposits a different energy as a result of how it interacts in a cell.

Once walk has been removed, the ToF peak will be cleaner, but still Gaussian-like. This is mainly due to two factors: tiny random fluctuations in the pulse-height signals, known as *jitter*, and the finite size of each detector. Jitter is instability in the input voltage pulse, which affects the generation of a fast logic pulse. The finite size of the cells in NSPECT contributes to measurement uncertainties because the exact location of detection cannot be determined; only the coordinates of the detecting cell are known.

The ToF circuits in D1 and D2 will each contribute to walk, and so the walk correction can be viewed as two separate corrections – one for each detector plane. D1_{C13} and D2_{C13} were selected for this analysis because of their location relative to the source

(they are on-axis, recall Figure 2.2). They are also expected to produce a Gaussian-like ToF distribution centered on 0 ns.

To determine how much walk is due to the D1 ToF circuit, only data where the energy deposited in D2 was between the ADC channel equivalents of 625 keV and 675 keV were selected. This range ensures that the majority of selected events resulted from Compton scattering of ^{60}Co γ rays. It is also approximately equal to the half-width-at-half-maximum (HWHM) from the instrument energy resolution [2]. One can therefore argue that, statistically speaking, energies within this selection are constant.

Data meeting the D2 pulse-height requirements were then divided into 50-keV sections based on the D1 pulse-height as demonstrated in Figure 2.10. The ToF for each section was plotted and fit using a Gaussian function. The resulting centroid ADC channel from the fit, and the weighted average pulse-height in D1 were recorded and plotted to determine the ToF walk in D1. The weighted average pulse-height of D2 was

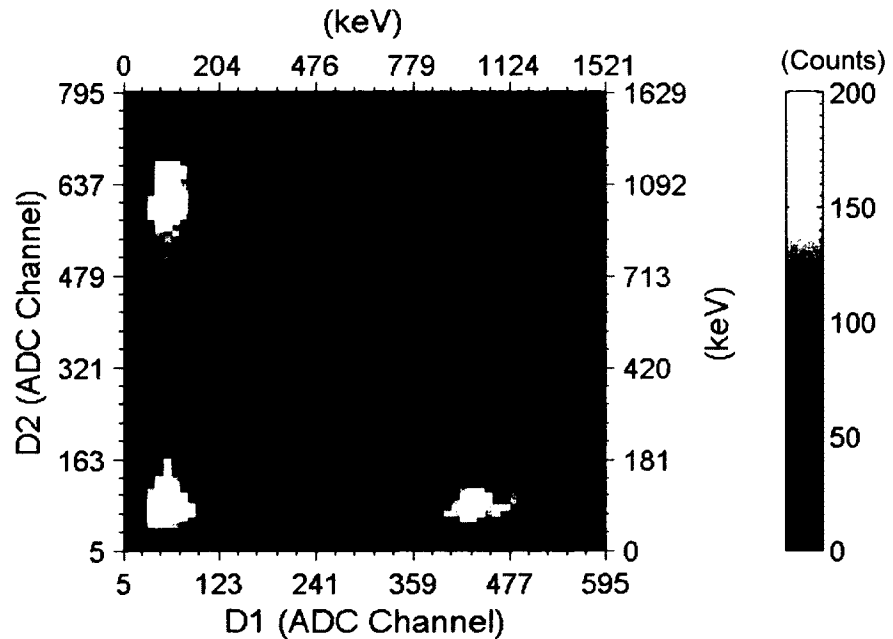


Figure 2.10. A density plot of the ^{60}Co energy spectrum measured with D1_{C13} and D2_{C13}. The blue (D1 fixed) and red (D2 fixed) boxes demonstrate how data were selected for the ToF walk analysis.

also calculated to confirm that it remained constant. This process was repeated to determine the walk from the D2 ToF circuit.

The results of this analysis are displayed in Figure 2.11. For both detector planes, the effect of walk becomes less significant at higher energies. The ToF versus pulse-height plots were translated so that higher energies corresponded to zero walk. The translated data, which now represent the ToF walk, were characterized using a cubic spline interpolation. Notice how walk causes the ToF to increase in D2 and decrease in D1 as pulse-height decreases. This is because delayed fast logic signals from D1 shorten the ToF while delayed signals from D2 increase the ToF.

Corrections may now be applied to all ToF measurements to remove pulse-height dependence. The walk correction is calculated for each detector plane using the cubic spline fits and the pulse-height channel in D1 and D2. Walk from D1 is then added to the ToF, and walk from D2 is subtracted.

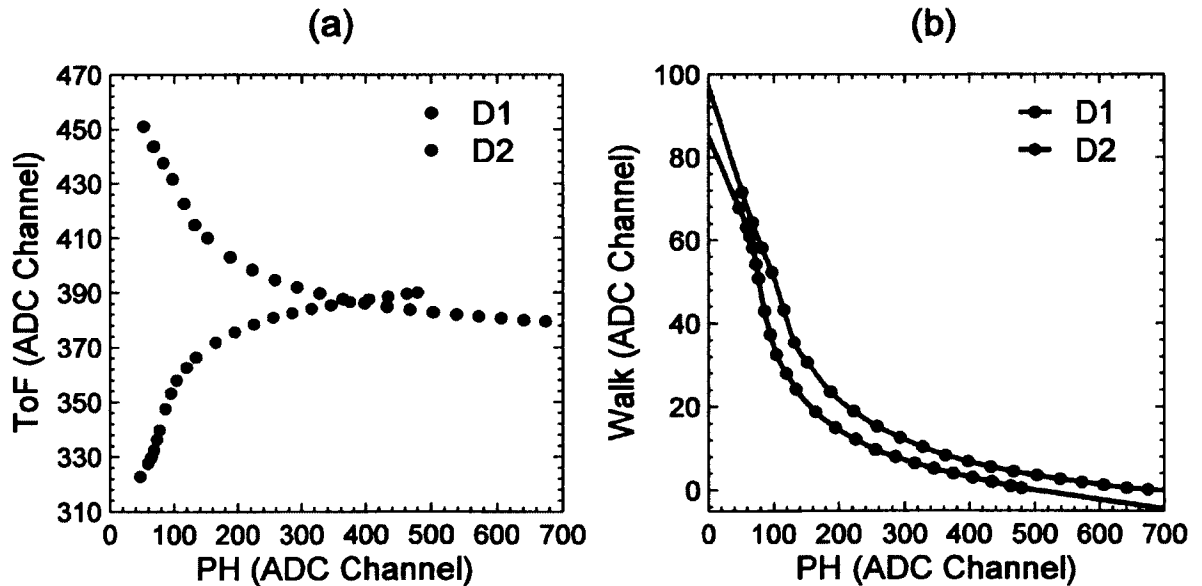


Figure 2.11. The fit results for the mean ToF versus the weighted average pulse-height (a). These data were translated to create the walk correction (b). Walk shifts the ToF by up to 70 channels in each layer.

2.5. Calibrating the Time-of-Flight Circuit

Three sets of data were taken with ^{22}Na in the same setup as the ^{60}Co source. ^{22}Na decays mainly via the emission of a positron, which annihilates with an electron to generate two 511-keV γ rays simultaneously. These γ rays are correlated because conservation of momentum requires that they are emitted in opposite directions.

All calibrations for NSPECT were carried out concurrently so that they would be completed in time to meet testing deadlines set in place by DTRA. Data acquisition during this period was mainly designated for the more labor-intensive energy calibrations because each cell had to be calibrated separately. Time for modifying the source setup and collecting data for the ToF calibration was therefore limited so it was desirable to have a higher count rate in D1_{C13} and D2_{C13}. The ^{22}Na source was selected because it emits correlated γ rays and it also had a greater activity than the ^{60}Co source.

For two of the three data runs, a cable was added to create an 8-ns delay in the

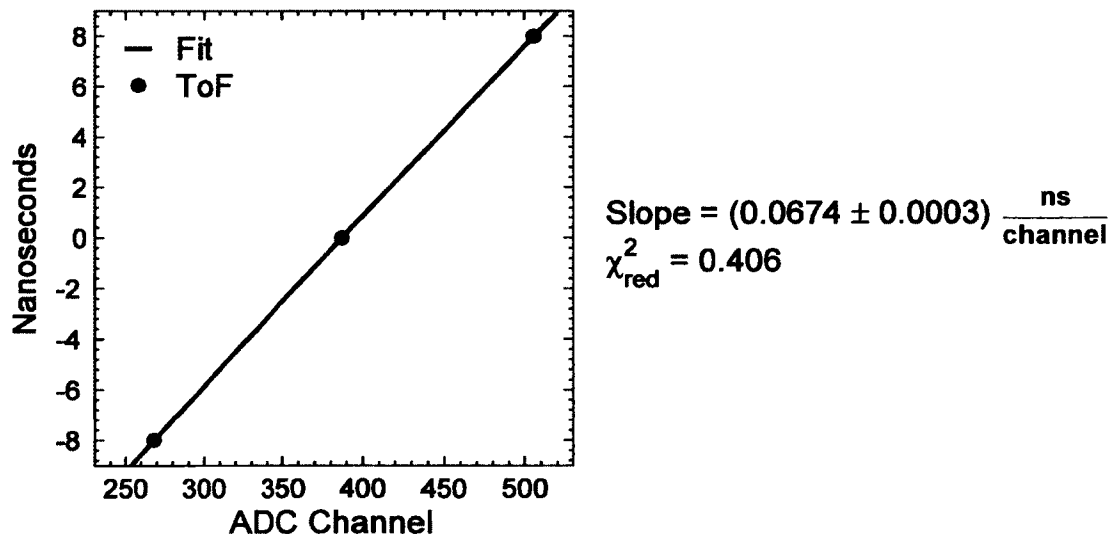


Figure 2.12. The ADC channel assigned by the TAC corresponds linearly to the time between two coincident events plus any delays introduced to the circuit. Calibration of the NSPECT ToF circuit resulted in a scaling factor of 14.8 channels per nanosecond.

signal that is fed to the ToF processing electronics. This delay was positive when the cable was added to the D2 sum board, and negative when added to the D1 sum board. No delay cables were added to the ToF circuit for the third data run.

Again using only $D1_{C13}$ and $D2_{C13}$, the ToF was corrected for walk and fit to determine the mean channel for each set of data. The centroids of the three ToF spectra were plotted with their respective delay cable time (-8 ns, 0 ns, and 8 ns). As can be seen in Figure 2.12, the relationship between ADC channel and time is linear. Fitting the three data points resulted in a conversion factor of approximately 14.8 channels per nanosecond.

2.6. Cell Electronics Offsets

Each cell introduces its own intrinsic delay which contributes to the systematic uncertainty in ToF measurements. These delays may be due to unequal cable lengths, small differences in the size and shape of the scintillator, PMT performance, preamplifier performance, and so on. The different delays cannot be separated so there is one combined delay, referred to as an *electronics offset*, for each cell that is the final correction to the ToF. The uniqueness of the electronics offsets means correcting the ToF depends on which cells detected an event.

The same ^{60}Co data used for the walk corrections were used to characterize the electronics offsets. The ToF data were walk corrected, calibrated to nanoseconds, and then sorted into forty-nine coincident cell combinations: twenty-five for $D1_{C13}$ with each cell in D2 and twenty-four for $D2_{C13}$ with each cell in D1 (except $D1_{C13}$). The uncorrelated nature of the γ rays emitted by ^{60}Co made it more favorable than ^{22}Na for this analysis.

To determine how the ToF fluctuates due to individual cell electronics, the data are also path length normalized. Path length normalization removes variations in the ToF due to different distances between cells as shown in Figure 2.13. This may be achieved by calculating the time for a γ ray to travel from the source to each cell in D1 and subtracting the time to D1_{C13}. The result, shown in Figure 2.14, is a correction that must be applied for each cell. The cell address numbering used in Figure 2.14 is shown in Figure 2.13. Due to symmetry, the path length normalizations in D2 are identical to those in D1.

All cell combinations were path length normalized to D1_{C13} because events between D1_{C13} and D2_{C13} have a known physical ToF of 0 ns. This correction was added to the ToF for the triggered cell in D1 and subtracted for the triggered cell in D2. At this point, all forty-nine plots would ideally have a mean ToF of 0 ns. Because no two cells are the same, the ToF peak for each plot was offset from 0 ns by some amount unique to the electronics of the cells that measured the data. These offsets, shown in Figure 2.16, were determined from Gaussian fits for forty-eight of the forty-nine ToF plots. The forty-ninth plot confirmed the 0-ns ToF between D1_{C13} and D2_{C13}.

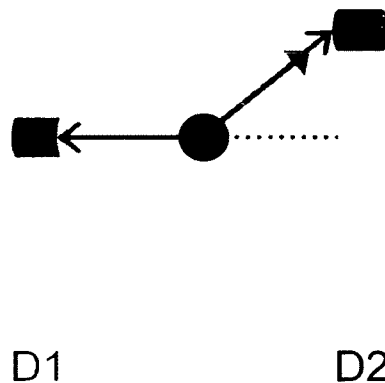


Figure 2.13. The bold orange arrow demonstrates how the path length to a cell in D2 differs from the path length to the central D1 cell. The ToF is normalized to account for this.

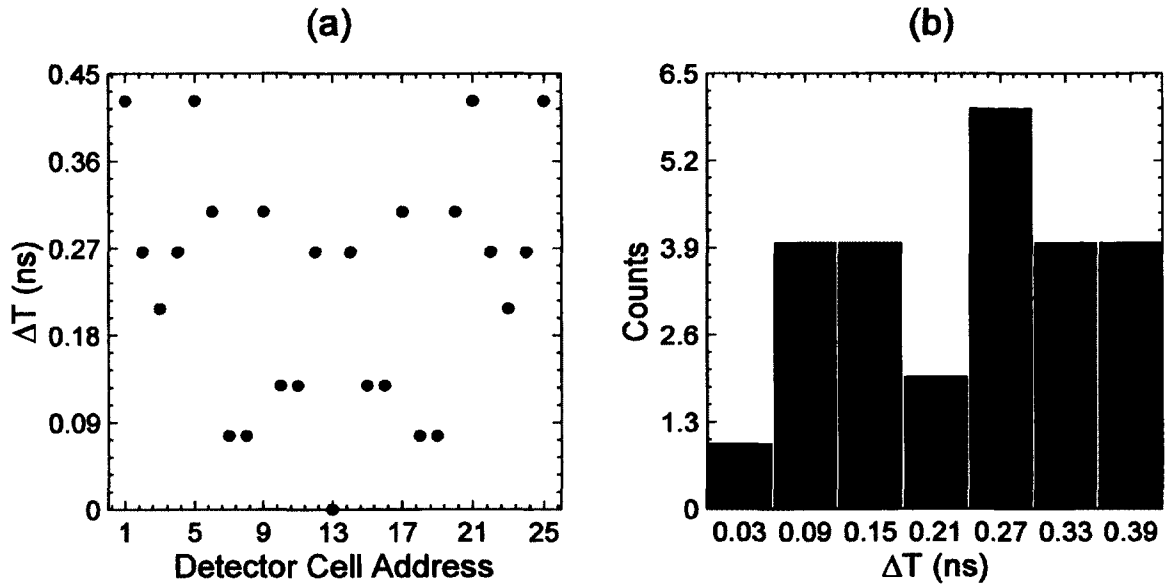


Figure 2.14. Scatter plot (a) and histogram (b) of the difference in γ -ray travel time (ΔT) due to path lengths from the calibration source to each cell in a detector plane. Normalization is achieved by subtracting ΔT from the ToF for each cell.

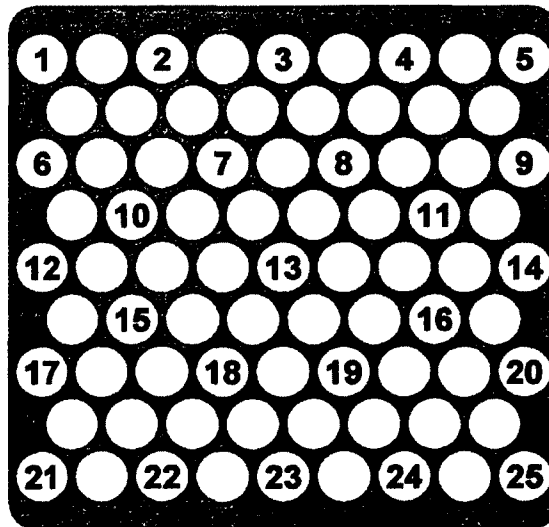


Figure 2.15. Cell address numbering is the same for all layers. In reference to the NSPECT coordinate system, the z -axis points into the page and the origin of the x - y plane is located at cell 13.

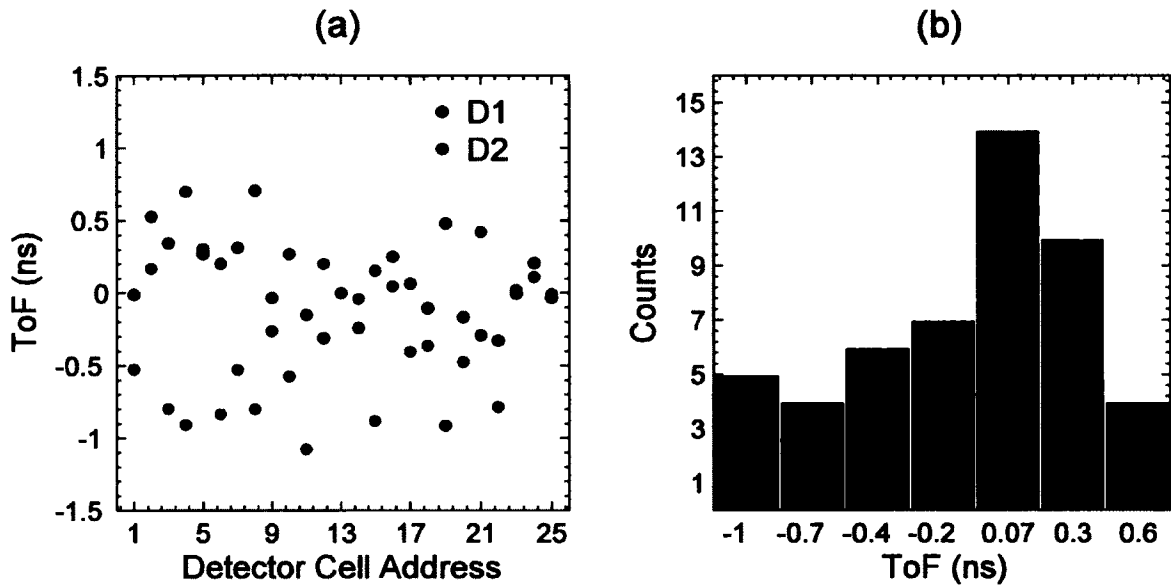


Figure 2.16. Scatter plot (a) and histogram (b) of the mean ToF for all forty-nine cell combinations. These values represent the electronics offsets for their respective cells in D1 and D2.

2.7. Fully Corrected Time-of-Flight Analysis

The ToF spectra after each correction are shown in Figure 2.17. These spectra were constructed from the ^{60}Co calibration data that were used for the majority of the ToF analysis in this chapter. The bin width and horizontal axis for each histogram were weighted using the calibration conversion from Section 2.5 to ensure that all histograms have the same scale. Notice the significant decrease in FWHM after the correction for electronics offsets. Good ToF resolution is desirable for obtaining high-resolution neutron energy measurements and consequently producing accurate source images.

Using the same process described in Section 2.4, now with all fifty cells, the fully corrected ^{60}Co calibration data were divided into $100 \text{ keV} \times 100 \text{ keV}$ sections to generate a grid that spanned from 0.2 MeV to 1.25 MeV. The ToF peak and FWHM were calculated for each section to determine the ToF dependence on the energy deposited in D1 and D2. The results are shown in Figure 2.18.

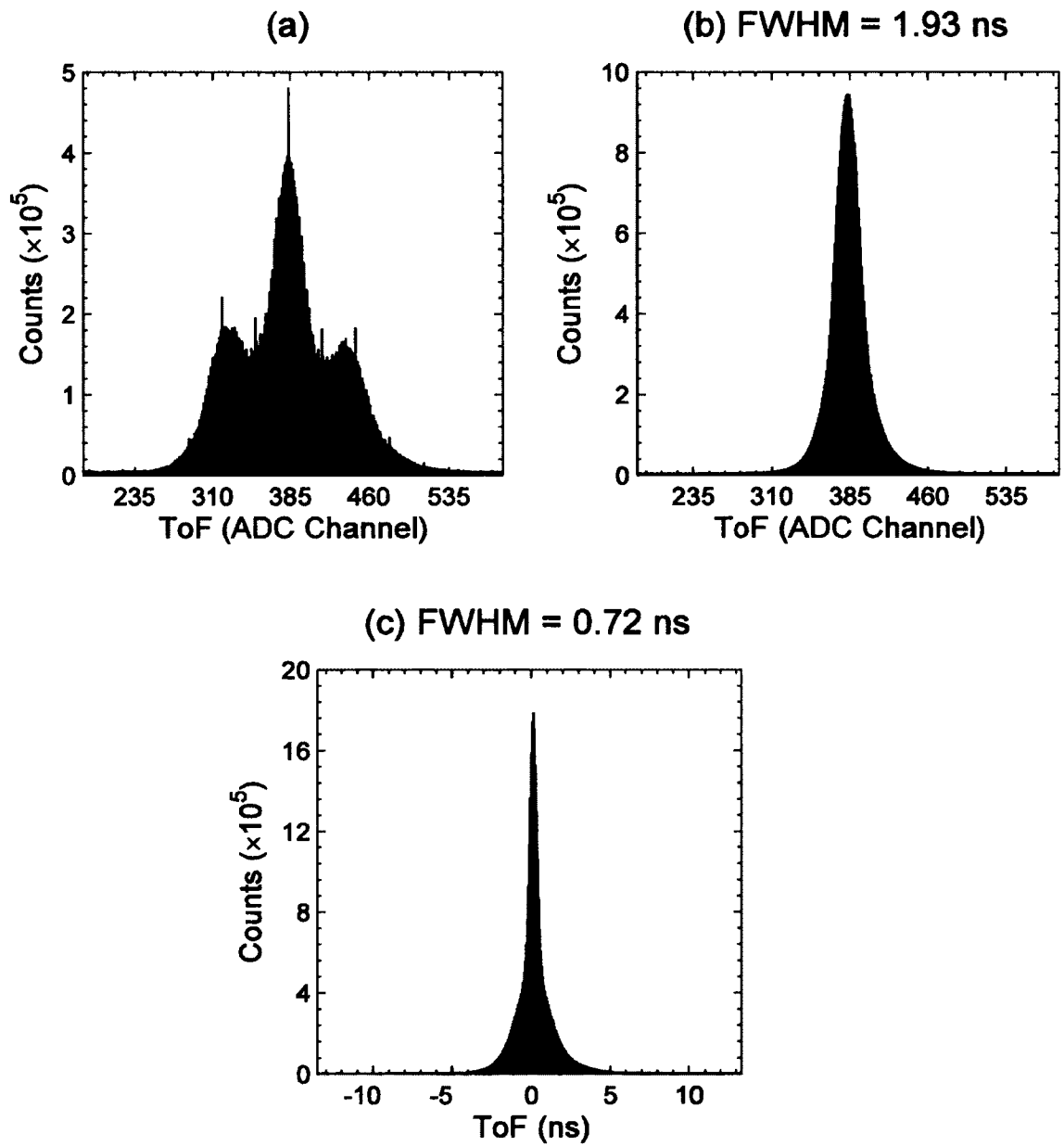


Figure 2.17. Progression of ToF corrections: (a) The raw ToF data obtained from NSPECT, (b) the walk corrected ToF, and (c) the fully calibrated and corrected ToF.

The energy range selected for this analysis minimizes contributions to the ToF from signals below 0.2 MeV and potential accidentals near or above the Compton edge. The ToF and ToF resolution vary dramatically in these two regions. The lower energy restriction avoids a large peak observed in the ^{60}Co energy spectrum. This peak is visible in both Figure 3.5 and Figure 3.6, and is likely caused by the detection of γ rays that have experienced additional scatters in the passive material surrounding the scintillators. Neither this peak, nor events with energies above 1.25 MeV, are part of the ^{60}Co Compton energy spectrum. Further discussion on the exclusion of these data is provided in the Appendix.

Figure 2.18 demonstrates the near-asymptotic decrease of the ToF resolution as energy increases. Before applying the walk correction, the ToF varied by about 4.7 ns (70 channels). Variations in the ToF are now less than 0.2 ns. Averages for the ToF and FWHM for these data are, respectively, 0.13 ns and 0.52 ns with standard deviations of 0.02 ns and 0.09 ns.

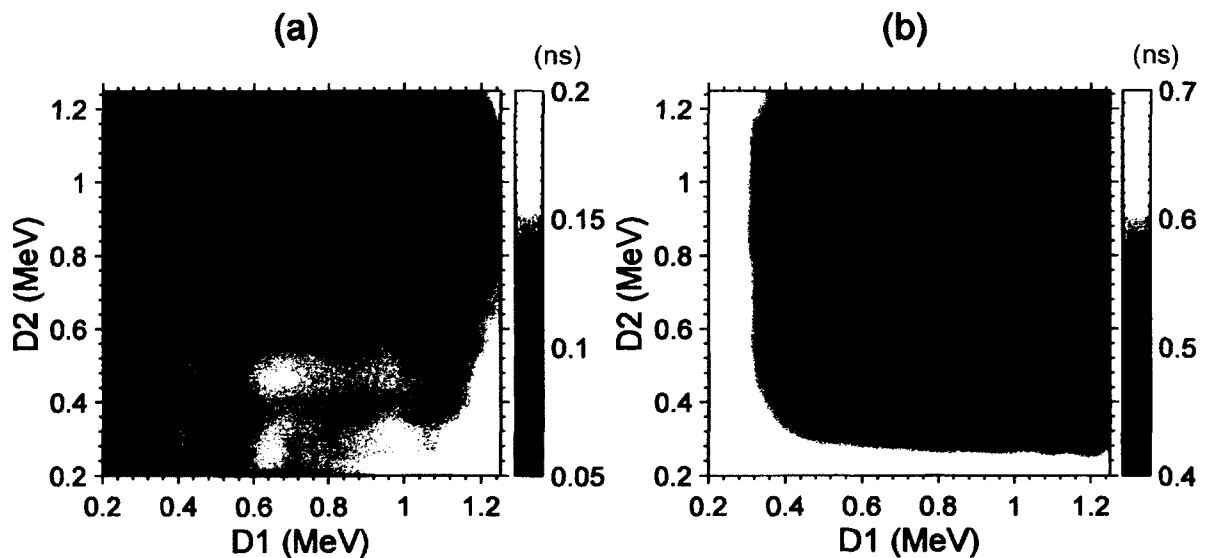


Figure 2.18. The fully corrected ToF and the FWHM as a function of the energy deposited in D1 and D2.

2.8. Neutron Detection

As mentioned in Section 2.1, proper treatment of particles detected between D1 and D2 requires the ability to distinguish neutrons from γ rays. The NSPECT software currently uses the pulse-shape-discrimination (PSD) properties in stilbene to achieve this. The ToF may also be used to identify the detected particle species but at the time of this writing has not yet been implemented in the software.

Scintillators fluoresce with prompt and delayed components as a result of the excitation of different states. These two components are responsible for the shape of the voltage pulse generated by the detector. The prompt component dominates the intensity of the scintillation output causing the signal to rise quickly. The delayed component causes the signal trail off slowly. In some scintillators, like stilbene, the slope of the slow component depends on the particle responsible for excitation. This produces a noticeable difference in the pulse shape. Measuring the ratio of rise time to decay time of the voltage pulse will result in a value that is unique to each type of detected particle. Running NSPECT with only γ -ray sources calibrates the PSD for γ rays so that later, events with γ -ray PSD values can be separated from the neutron data.

The ToF may also be used to separate neutron events from γ -ray events. Neutrons travel from D1 to D2 with subluminal velocities, while γ rays travel at the speed of light. The neutron ToF will therefore be significantly greater than the γ -ray ToF. For example, the distance between D1 and D2 is about 37 cm. A γ ray will cover this distance in about 1.25 ns. Neutrons with energies ranging from 0.5 MeV to 15 MeV (velocities from 0.03c to 0.18c) travel the same distance in about 38 ns to 7 ns. This allows for a lower limit to be placed on the neutron ToF.

The fully corrected ToF is used in (2.1) to calculate the kinetic energy (E_T) of a detected neutron as it travels from D1 to D2.

$$E_T = \frac{1}{2} m \left(\frac{L}{t} \right)^2 \quad (2.1)$$

In this equation, L is the distance between cells and t is the ToF. It should be noted that this calculation is only valid for neutrons because relativistic effects have been ignored. Compton scattering must be considered for γ rays. The PSD and ToF methods described above allow neutrons to be distinguished from γ rays so that energy calculations are handled appropriately.

The total energy of an incident neutron (E_n) will be the sum of E_T and the energy it loses in D1. Hence the neutron energy resolution (FWHM/ E_n) depends on the energy resolution of D1 and the ToF resolution. These values are correlated because the D1 energy resolution affects the timing of fast logic pulses from the CFD. This means the propagation of errors to obtain the incident neutron energy resolution must be carefully conducted. The variance in scattered neutron energies (σ_T), shown in (2.2), was derived using (2.1) where σ_t^2 is the variance in the ToF from Section 2.7 ($\sigma_t^2 = 0.0938$ ns).

$$\sigma_T^2 = \left(\frac{\partial E_T}{\partial t} \right)^2 \sigma_t^2 = \left(\frac{mL^2}{t^3} \right)^2 \sigma_t^2 \quad (2.2)$$

2.9. Final Remarks

At the time of this writing, all ToF corrections have been successfully integrated into the NSPECT software. The ToF must be checked occasionally to determine whether these corrections are still valid. Testing the ToF system requires taking measurements with a γ -ray source placed according to specifications provided in Section 2.4. Data collection time will depend on strength of source.

Currently, analysis is done manually with separate code where the fully corrected ToF peak is fit and then inspected visually. This testing process can be automated to some extent, and it is possible to include it in the NSPECT software with occasional prompts for the user. This section outlines the possible issues to look for when testing the ToF corrections, a procedure for addressing these issues, and how one might automate such a process. The order in which these issues are presented is the order that the automated software should use for testing and fixing.

First and foremost, the user will need to specify that the source is in the calibration setup to initiate the testing software. This is important for the application of the correct path length normalization. If the user does this, the NSPECT software should perform all original ToF corrections, storing the results of each correction separately to facilitate the analysis of each correction step. A plot of the ToF after each correction step will be displayed once the corrections are complete for a quick comparison to Figure 2.17. If the user does not specify the calibration setup, the NSPECT software will proceed with its full data analysis. Regardless, the data acquired for each event, and their corrections, will be output to an ASCII file.

The figures generated during testing allow the user to visually inspect the ToF correction steps. At this point, the user may decide if there are a sufficient number of events to fit the ToF with a Gaussian function or if a longer data acquisition time is required. The user may also decide to skip additional tests and keep the ToF corrections or immediately start re-doing them. If the user elects to continue with analysis, the user must indicate which step the software will check in greater detail. This software will access the ASCII file created by NSPECT.

2.9.1. Checking NSPECT Hardware

Careful measurement is required to place the test source, so it should be evident if detector planes have shifted. Such a shift will directly affect the path length normalizations and will therefore be visible in all ToF spectra. It will also have an effect on the imaging analysis results.

In the event that the detection layers have shifted, the user will have to readjust the detection layers to original specifications or measure the distance between detection layers and change this value in the software. The distances between detector planes could be an option in the software that can be modified by the user, in which case the software would need to be capable of adjusting the predefined cell coordinates accordingly. Regardless of the chosen method for fixing a shift in detector planes, they will need to be secured and the source of the shift must be identified. If no damage is visible (such as broken wires), it is highly recommended the user proceed with additional ToF checks to ensure that the electronics were not affected.

2.9.2. Checking Walk Correction

For an in-depth check of the walk correction, the software should loop through the walk corrected data (with no other corrections applied), dividing the data into sections of pulse-height to check the ToF peak position as described in Section 2.4. For each section, the software will perform a Gaussian fit on the ToF from ADC channel 363 to ADC channel 411 (a range of approximately $4\sigma_t$ centered on expected 0 ns peak, converted to ADC channels) and output plots of the fitted ToF peak. The software will pause after each section so the user can verify the accuracy of the fit. At this point the user may elect to adjust the fit range, halt analysis, or continue to the next pulse-height section.

The ToF peak should not vary more than 14.1 channels (approximately equal to the HWHM at this step), and the software should automatically check this. In the event that the ToF does vary significantly, the user will be notified that the walk must be re-done. The user may decide at any time to re-do the walk correction based on visual inspection of the plots.

The code used to determine the walk correction in Section 2.4 is available but more development is required for automation. The automated code should save the current fit parameters and the corresponding weighted average pulse-heights before proceeding so past versions may be restored if necessary. A plot similar to Figure 2.10 should be generated to assist the user in defining pulse-height sections.

For each section of pulse-height data, the ToF will be plotted and the user prompted to specify a range for fitting. The fit will then be displayed over the plot. The user should have the option to perform the fit with a new range in the event that the previous fit is unsatisfactory. This manual specification of the fit range is necessary to

ensure that it does not include the wings seen in the raw data (recall Figure 2.17), which would skew the fit results significantly. Once satisfied, the user must type a command to continue to the next pulse-height section.

Once all pulse-height sections have been stepped through, the code will perform the necessary cubic spline interpolations. Cubic spline interpolations have not yet been integrated into the walk analysis code (Ralph H. Pennington's *Introductory Computer Methods and Numerical Analysis* provides a good example for how to do this). The results will be plotted for the user to compare to Figure 2.11. Significant differences may indicate an issue in the electronics that is beyond the scope of this thesis. Acceptable results should be output as an ASCII file that will replace the current walk correction file used in the NSPECT software.

2.9.3. Checking Calibration to Nanoseconds

Checking the conversion from ADC channel to nanoseconds requires at least three data runs. The source need not be moved, but each data run will require a different delay cable, as described in Section 2.5. This check assumes the walk correction is good and so the process described in 2.9.2 is skipped.

Data must be acquired for each delay cable and run through the initial correction software to create an ASCII file. The walk-corrected ToF for each data run is fit with a Gaussian function, where the user must specify the range. Automated software can apply the current conversion to nanoseconds for each peak and compare the result to the expected delay cable time. The user should be alerted if these values differ by more than 0.95 ns (approximately equal to the HWHM at this step).

If a new calibration is required, the software should automatically save the current conversion to nanoseconds so past versions may be restored if necessary. As described in Section 2.5, the conversion from ADC channel to nanoseconds requires the ToF peaks from walk-corrected data. Code that calculates this conversion and plots the results is available; but just like the walk correction code, more development is required for automation. The conversion from ADC channel to nanoseconds should be linear, requiring only three data points (recall Figure 2.12).

In the event that the conversion is nonlinear, additional data points can be obtained using delay cables with different lengths. If a linear relationship is not visible between ADC channel and the delay cable time after including several data points, there may be issues with the electronics that are beyond the scope of this thesis. If deemed acceptable, the new channel-to-nanoseconds conversion should automatically be applied to the NSPECT software.

2.9.4. Checking Electronics Offsets

The software to check the electronics offsets should loop through all the cell combinations described in Section 2.6. The data being analyzed should be the fully corrected. For each cell combination, the ToF will be fit with a Gaussian function from -0.61 ns to 0.61 ns (a range of approximately $4\sigma_t$ centered on expected 0 ns peak). The fitted ToF will be plotted for the user to inspect.

As in 2.9.2, the software will pause after each section so the user may verify the accuracy of the fit. The user has the option to adjust the fit range, halt analysis, or continue to the next cell combination. The ToF should not vary more than 0.35 ns

(approximately equal to the HWHM at this step) for each cell combination. The software should check for this and notify the user in the event that it does.

Fixing the electronics offsets requires walk-corrected, calibrated, and path length normalized data. The code used in Section 2.6 is available, but it does need some modifications to make it automated. The current fit parameters and the corresponding cell IDs should be automatically saved before proceeding so past versions may be restored if necessary.

For each cell combination, the ToF is plotted and the user prompted to specify the fit range. The fit will then be added to the plot. The user should have the option to perform the fit with a new range in the event that the previous fit is unsatisfactory. The user must type a command to continue to the next cell combination.

A plot of the fit results should be generated for comparison to Figure 2.16. It should be evident from the ToF plots, among other things, if a cell is not functioning properly. Acceptable results should be output as an ASCII file that will replace the current electronics offsets file used in the NSPECT software.

NOTES

1. From Glenn F. Knoll, "Pulse Shaping, Counting, and Timing," pp. 682 - 687. *Radiation Detection and Measurement*, 4th Edition. Copyright © 2010 by John Wiley & Sons, Inc. This material is reproduced with permission of John Wiley & Sons, Inc.
2. From William R. Leo, "Timing Methods and Systems," p. 328, in *Techniques for Nuclear and Particle Physics Experiments: A How-to Approach*, 2nd Edition. Copyright © 1994 by Springer-Verlag Berlin Heidelberg. With kind permission of Springer Science + Business Media.

3. AN INSTRUMENT FOR THE ASSAY OF NUCLEAR REACTOR FUEL

A new design based on the NSPECT instrument is proposed for the assay of spent nuclear reactor fuel. This design is a simplified form of the NSPECT neutron detection layers. The proposed neutron detector consists of two cells, as shown in Figure 3.1, making it more portable than NSPECT. It is also more readily optimized to obtain high-resolution energy measurements. This allows for control over which features in the neutron energy spectrum are measured in detail. The time-of-flight (ToF) calibration for this instrument follows the same procedures outlined in Chapter 2 with the exception of Section 2.6; corrections for electronics offsets are unnecessary with only two cells.

The advantage of using an instrument such as NSPECT for analyzing spent fuel is the sample can be examined without removing it from storage. This would provide much insight into current storage methods and reduce the safety hazards involved in inspecting waste materials or monitoring for contamination. The instrument may also be operated by a single technician. This chapter discusses the optimization and applications of such a device.

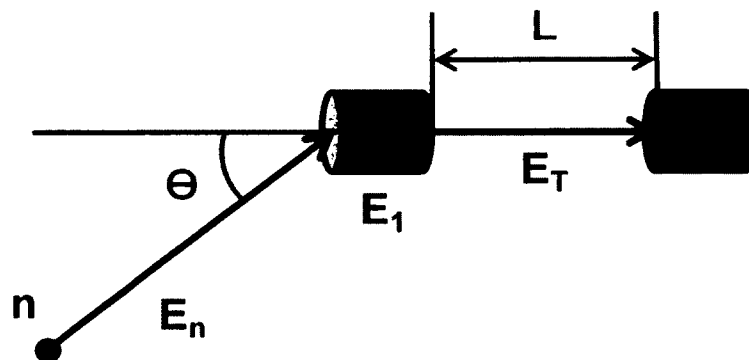


Figure 3.1. A model of the proposed neutron detector. A neutron with incident kinetic energy E_n deposits energy E_1 as it scatters in D1. The scattered neutron travels with a kinetic energy E_2 to D2.

Neutrons have the greatest range of all radiation from reactor fuel. As a result, neutrons may originate from any part of the fuel, while γ rays only escape from a thin layer on the surface and α particles seldom escape at all. An assay of neutrons emitted from spent fuel could potentially be used to determine the isotopic composition or activity of the fuel as a whole.

3.1. *A Summary of Nuclear Power Reactor Theory*

A power reactor is a nuclear reactor that generates mechanical energy from the fission products of the fuel. According to the International Atomic Energy Agency, there are 434 nuclear power reactors in operation today [3]. These reactors are designed for the large-scale production of electricity for grid distribution.

Approximately ninety-six percent of the power reactors in operation worldwide are thermal reactors that rely on induced fission by thermal neutrons ($E \sim 0.025$ eV). Thermal power reactors convert the heat generated from the interaction of fission products into steam. The steam is fed into a turbine that is connected to an electric generator.

This section provides a brief discussion of the physics of nuclear fission and thermal power reactors. The designs of the two most common thermal reactors are also discussed. Finally, current safety and waste management procedures are examined.

3.1.1. Nuclear Fission Physics

Fission is the splitting of an unstable heavy nucleus into at least two smaller nuclei known as fission fragments or daughter nuclei. This process is accompanied by the release of neutrons and γ rays. The majority of neutrons, called prompt neutrons, are emitted within approximately 10^{-14} seconds of fission. Several seconds to minutes after

fission, the daughter nuclei decay to lower excited states. The decay of fission fragments is most commonly achieved via the emission of γ rays, but occasionally they beta decay to an excited state that is energetic enough for the emission of a delayed neutron. Of the total number of neutrons emitted per fission, approximately 99% are prompt neutrons and 1% are delayed neutrons.

Immediately after fission, the two fragments each possess an excess of neutrons and are in a highly excited state. The fission fragments instantly evaporate excess neutrons (prompt neutrons) to reach lower excited states. At these energies, the Fermi-gas model predicts a large density of states. Because the nuclear states are packed so closely together, the distribution of these states is approximately continuous.

Like γ decay, neutrons are produced from radioactive decay with energies characteristic to the separation between nuclear excited states. This means that the prompt neutrons should be produced with discrete energies that are related to the nuclear states they vacated. A continuous distribution of states in the fission fragments means that the prompt neutrons may also have a continuous distribution of energies. This is why a wide range of energies are observed in neutron energy spectra from fission sources. It should be noted that this does not necessarily mean all energies are equally probable.

Very few isotopes in nature fission will spontaneously. Spontaneous fission only becomes possible for nuclei with large mass numbers. In these nuclei, however, α decay is the more probable method of decay. This is because the Coulomb potential barrier is smaller for α particles than the more massive fission fragments.

Fission can be induced in some heavy nuclei as a result of neutron capture. If a heavy nucleus captures a neutron, it can be excited such that – according to the liquid

drop model – its spherical shape is distorted. If the nucleus is sufficiently deformed, Coulomb repulsion will exceed the nuclear binding force and the nucleus will split.

The amount of energy required for fission fragments to overcome the Coulomb barrier and separate is called the activation energy. This energy is estimated using the liquid drop model. The minimum energy for a neutron to induce fission may be estimated by subtracting the excitation energy of a nucleus after it captures a neutron from the activation energy of the resulting compound nucleus. The necessary neutron energy for induced fission of ^{235}U and ^{238}U are approximated in (3.1), where the calculated activation energies for ^{236}U and ^{239}U are 6.2 MeV and 6.6 MeV, respectively [4].

$$E_n = E_A - [M(^{235}\text{U}) + M_n - M(^{236}\text{U})]c^2 = -0.34 \text{ MeV} \quad (3.1)$$

$$E_n = E_A - [M(^{238}\text{U}) + M_n - M(^{239}\text{U})]c^2 = 1.8 \text{ MeV}$$

The results from (3.1) demonstrate how ^{235}U can, in theory, fission by capturing stationary neutrons while ^{238}U requires neutrons with energies greater than 1 MeV. Measured cross sections for neutron-induced fission of uranium isotopes are in agreement with these results [1]. While neutron-induced fission of ^{235}U may occur at any energy, cross sections are much higher at thermal energies. Neutron-induced fission cross sections for ^{238}U are orders of magnitude smaller than ^{235}U at thermal energies.

3.1.2. Fission Power Reactors

The energy released during fission is significantly greater than the energy required to induce the reaction, which is why fission is a desirable method for energy production. Most of the energy released during fission is carried away as kinetic energy by the daughter nuclei. The remaining energy is carried away by other decay products

such as neutrons and γ rays. Heat is generated as the fission products transfer their energy to various materials in the reactor. Power reactors harness this heat and convert it to steam to spin a turbine.

The fissionable material used in power reactor fuel today is uranium. The energy released during fission of ^{235}U is approximately 200 MeV. This is much greater than the energy of the thermal neutron that induced fission. Two methods for estimating the energy released via the fission of ^{235}U are demonstrated in (3.2) and (3.3). The first method calculates the quality factor using rest-mass energies of the particles involved in the reaction. The second method uses the semi-empirical mass formula to calculate the binding energies.

$$\begin{aligned}
 &^{235}\text{U} + n \rightarrow ^{93}\text{Rb} + ^{141}\text{Cs} + 2n \\
 E &= [M(^{235}\text{U}) - M(^{93}\text{Rb}) - M(^{141}\text{Cs}) - M_n]c^2 \approx 182 \text{ MeV}
 \end{aligned}
 \tag{3.2}$$

$$\begin{aligned}
 &^{235}\text{U} + n \rightarrow ^{145}\text{Ba} + ^{94}\text{Kr} \\
 E &= B_{145} + B_{94} - B_{235} \approx 245.9 \text{ MeV}
 \end{aligned}
 \tag{3.3}$$

It should be noted that (3.2) and (3.3) are not exact and are merely meant to show that the energy released in each of the above fission reactions is approximately 200 MeV. In particular, only the first three terms of the semi-empirical mass formula were used in (3.3), which is sufficient for obtaining the correct order of magnitude. Also, to make (3.2) more accurate, one would need to know the initial kinetic energies of the parent nucleus, incident neutron, and fission products.

3.1.3. Neutron Moderation and Reactor Criticality

Fission in a nuclear reactor must result in the release of at least one neutron that induces fission. This, by definition, is a chain reaction. The neutron reproduction factor (k) is an estimate of the number of prompt neutrons, produced from a single fission event, available to induce fission. For a reactor to maintain a chain reaction and produce a constant power output, k should ideally be one. The state of a reactor is categorized into three groups based on the neutron reproduction factor. A reactor is subcritical if k is less than one, critical if k is one, and supercritical when k is greater than one.

A fissioning nucleus will, on average, emit two highly energetic prompt neutrons. In thermal reactors these neutrons must be moderated (slowed down) to thermal speeds, which increases the probability that they will induce fission. To conserve the number of neutrons available to fission, moderators are composed of relatively light elements that have large cross sections for neutron elastic scattering and a small cross section for neutron absorption.

Some neutrons will be absorbed during the moderating process as they interact with materials in the reactor core. The neutron reproduction factor accounts for all major losses that may occur during moderation of prompt neutrons. These include: (1) the large resonance capture cross sections of ^{238}U , (2) neutron absorption by various materials within the reactor, and (3) the escape of neutrons from the reactor core.

Reactor fuel assemblies include space for control rods with high neutron-absorbing materials to regulate criticality. Even with the control rods, it is extremely difficult to maintain k of exactly one. Supercritical reactors require rapid regulation to control the number of neutrons emitted during fission, which can be challenging and

unsafe. Subcritical reactors are preferred because they depend on the release of delayed neutrons, which are not accounted for in k . The slow release of delayed neutrons allows for a more realistic response time with control rods.

3.1.4. Power Reactor Design

Nuclear power reactors must maintain a power output consistent with consumer demand by regulating neutron production. They must also include numerous redundancies so that if a system fails, the reactor will remain subcritical. Materials-related decisions when designing a thermal power reactor may include: what type of fuel should be used, what moderator will work best, how the reactor core should be cooled, and how the energy should be extracted to generate electricity.

Uranium is currently the most cost-effective fissionable material to acquire and process into reactor fuel. It is found naturally as an ore in great abundances. The main isotopes found in natural uranium are ^{238}U and ^{235}U with abundances of 99.3% and 0.7% respectively. Mined uranium ore is processed into a powder, typically uranium dioxide (UO_2), which is compressed and fired to form pellets. These pellets are sealed into the reactor fuel rods. Depending on the reactor size, there could be between 200 and 800 fuel assemblies each with 90 to 300 fuel rods.

Thermal reactors are the most common type of power reactor. These reactors were designed to take advantage of the large cross sections of ^{235}U for induced fission by thermal neutrons. Uranium used in thermal reactors is often enriched to increase the ^{235}U abundance to about 3%. Moderator choices include water and graphite, the most popular being water.

Heavy water, which contains two deuterium atoms instead of hydrogen, is used in some reactors today because, compared to light water, it is less likely to absorb neutrons. This reduces the need for enriched uranium to account for absorption losses. It is expensive to produce though, which significantly offsets the reduced cost of using natural uranium. On the rare occasion that heavy water does absorb a neutron, hazardous materials such as tritium are produced and must be carefully disposed. For economic and security reasons, light water is usually preferred to heavy water for moderating nuclear reactors.

Heat is generated in a reactor as fission products transfer their kinetic energy to various materials in the core. The heat is extracted by cycling a working fluid through the core. The main function of the working fluid is to cool the core to prevent a meltdown. During operation, the working fluid also powers a turbine, either directly or indirectly, to generate electricity.

Thermal reactors today use water as the working fluid and steam to power turbines. There are essentially two major methods used in thermal reactors for steam production. The first is to directly boil the water in the reactor core and feed the resulting steam to the turbine. The second is to cycle water under high pressure through the reactor core in a closed loop which exchanges heat with water flowing through a separate closed loop. Steam is produced in the second closed loop and is fed to the turbine. The second method tends to be more popular because the closed loops reduce the risk of radioactive material escaping the reactor core.

3.1.5. Neutron Poisons

Fission products in reactor fuel build up over time, and many of them have large cross sections for neutron capture. These fission products are called neutron poisons. Neutron poisons cause a significant decrease in the neutron reproduction factor which affects reactor operation. Control rods are used in the reactor core to reduce the effect of the fluctuating amount of neutron poisons and maintain a constant power output.

The main neutron poison that affects reactor operation is ^{135}Xe . Produced from the decay of ^{135}I , and occasionally directly from ^{235}U fission, ^{135}Xe is the most abundant fission product. It also has the highest thermal neutron capture cross section of all neutron poisons. During operation, ^{135}Xe either captures a neutron to become stable ^{136}Xe (burn-up) or decays to long-lived ^{135}Cs , the former being the most common [5]. Neither ^{136}Xe nor ^{135}Cs have large cross sections for neutron capture.

During operation, ^{135}I and ^{135}Xe build up in the reactor core until equilibrium is reached. The reactor can maintain a constant power output with ^{135}Xe at equilibrium. Changes in the power level present a problem because the amount of ^{135}Xe changes such that the reactor must be carefully controlled. When the power level is decreased, the ^{135}Xe production exceeds burn-up, and the ^{135}Xe concentration peaks. Conversely, increasing the power level results in a drop in ^{135}Xe as burn-up exceeds production.

Power reactor control systems must carefully adjust power levels to meet fluctuating demands from the grid. With a buildup of ^{135}Xe , a rapid decrease in power could cause the criticality to drop enough that the reactor shuts down completely. This is an issue because the reactor cannot be restarted until a sufficient amount of ^{135}Xe decays to ^{135}Cs . A rapid increase in power could result in supercritical conditions and possibly

lead to core meltdown. The solution to these problems is twofold: (1) Change the power level in small steps to prevent changes in ^{135}Xe abundances that cannot be countered by control rods, and (2) allow excess steam to bypass the turbines during periods of low demand to allow the reactor to operate at constant levels rather than power down.

The second most prominent neutron poison is ^{149}Sm , which is produced from the decay of ^{149}Pm . Unlike ^{135}Xe , ^{149}Sm is stable to decay and captures neutrons to form additional neutron poisons. During operation, ^{149}Sm builds up until equilibrium is reached. Fortunately this equilibrium is independent of power level changes because ^{149}Sm is produced in much smaller quantities compared to ^{135}Xe . It does, however, have a small effect on reactor start-up and shut-down in much the same way as ^{135}Xe .

In the United States, and other nations, neutron poisons are not extracted from reactor fuel. Extraction would require breaking down fuel assemblies, unsealing the fuel rods, and removing the depleted UO_2 pellets for reprocessing. Neutron poisons must therefore either decay or burn up in the fuel. Concentrations of neutron poisons fluctuate during reactor operation which affects the control of power output. Eventually, the presence of neutron poisons, combined with the decreased abundance of fissionable material, results in neutron production so low that the desired power output cannot be sustained.

3.1.6. Waste Management

After four to six years in a reactor, it becomes economically necessary to replace fuel assemblies in order to maintain the reactor efficiency. The refueling process is staggered so that about one-quarter to one-third of the fuel assemblies are replaced every one to two years. Refueling is typically done in the spring or fall when demand for

electricity is low because the reactor must be shut down. Upon removal from the reactor core, spent fuel assemblies still produce significant amounts of heat. They are transferred to large pools of water (wet storage) where they are kept cool and shielded.

The United States and several other nations are reluctant to adopt reprocessing or permanent storage of spent fuel. As a result, spent fuel must be stored on-site or in temporary buildings close to the reactor. Concerns over the safety and available space of wet storage has led to the development of dry storage, in which thirty to seventy fuel assemblies (all in wet storage for at least five years) are encased in multi-layered casks of steel and concrete. Dry storage frees up space in wet storage for newer fuel assemblies and allows the spent fuel to be housed separately from the reactor building. It has yet to be determined whether dry storage is more cost-effective or safer than wet storage, as it introduces new challenges for establishing policies.

3.2. Applications for Proposed Detector

Neutron assay of spent fuel assemblies can provide insight into the isotopic composition of irradiated fuel. Only a handful of research facilities in the United States currently examine spent fuel. Testing at these facilities include (1) determining the fuel quality, (2) monitoring for damage in the fuel assemblies, (3) determining the severity and cause of failures in reactor components under normal operation, and (4) inferring the behavior of a reactor in an accident. Transportation of fuel assemblies to these facilities must be executed with caution. A complete analysis will take time, but is useful in the long-term for improving the development of reactor components, storage techniques, and safety protocols.

A portable device for on-site assay of neutrons could provide real-time information critical for reactor safety and efficiency. This device could help determine the effectiveness of storage methods for spent fuel by measuring radiation activities from outside the containers. The assay of neutrons is also useful for the location of missing sources or contamination. In facilities where radioactive material is handled, such as a nuclear power plant, radiation can build up in various locations. Surveys must be completed regularly to monitor for buildup. A device for detecting neutrons would allow an operator to survey high-density materials, such as lead pipes, where γ rays cannot escape.

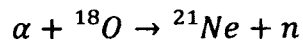
The design of a neutron detector, based on the NSPECT instrument, is proposed in this chapter for the assay of spent nuclear fuel. This device must be compact and user-friendly so that it can be easily operated. Because some applications may require it to function in high temperatures or in water, remote control capabilities may be desirable to reduce the personnel hazards.

The advantage of basing this device on NSPECT is that the design is adaptable. It could, in theory, be calibrated for operation with several types of scintillation detectors. The detector cells could be exchanged depending on whether the operator wants to detect neutrons or γ rays, for example. The separation between cells would be adjustable to tailor the energy resolution and efficiency to the desired application. These properties would reduce the number of devices required to complete safety surveys.

Spent fuel can remain highly radioactive for thousands of years. The radiation that escapes spent fuel most often are neutrons and γ rays. Neutrons may originate from any

part of the fuel, while γ rays emanate only from a thin layer on the surface due to a higher cross section for absorption.

Neutrons in UO_2 fuel are produced from fission and from (α, n) reactions, where α particles combine with oxygen (typically ^{18}O) to produce a stable isotope of neon and one free neutron.



Neutrons from (α, n) reactions in UO_2 are produced at a rate less than or equal to delayed neutrons from fission and so they will have a small contribution to reactor criticality.

The compound nucleus formed by an oxygen nucleus and α particle is much smaller than the daughter nuclei produced from fission. As discussed in 3.1.1, the size of this compound nucleus does not allow for a continuous distribution of states. This means there are a discrete set of possible energies with which the compound nucleus can emit a neutron. With a sufficient number of α emitters in the fuel, and good energy resolution, these neutrons (which have a much smaller range of energies than prompt neutrons) should be visible as an irregularity in the fission count spectrum (illustrated in Figure 3.2).

After measuring neutron energies with the proposed device, the fission count spectrum could be subtracted much like a background measurement. The remaining spectrum provides a measure of the number of neutrons produced from (α, n) reactions. It is unlikely that an α particle will escape the reactor fuel, and so the number of neutrons produced from reactions with oxygen is an estimate of the number of α emitters present. Determining the exact number of α emitters in the fuel requires consideration of α -particle interactions with nuclei other than oxygen.

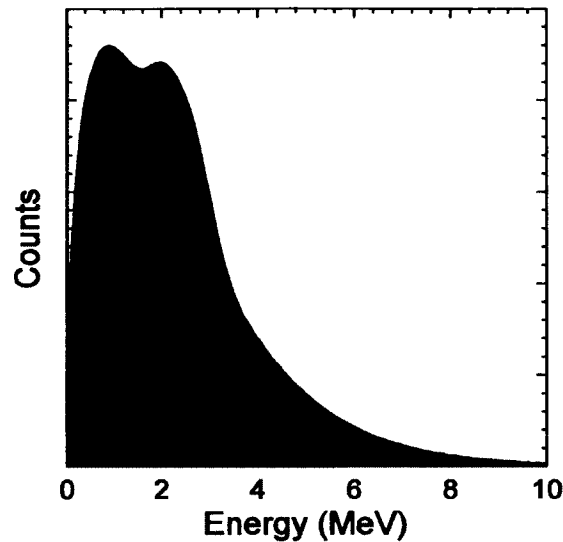


Figure 3.2. Illustration of how (α, n) reactions in UO_2 fuel might modify the fission spectrum. The solid red line is the fission spectrum. The dashed green line is what might be revealed if the fission spectrum was removed.

The fission count spectrum to be subtracted out is obtainable from fresh fuel that has not yet been irradiated in the reactor core (no accumulation of α -emitting poisons). Some analysis and testing is required to determine the correct intensity of the fission spectrum. This analysis must account for the decreased activity of the fissionable material in the spent fuel. An algorithm may then be produced which generates the fresh fuel equivalent of the spent fuel count spectrum.

Detector portability enables the assay of nuclear fuel without needing to move or disassemble fuel assemblies. When it is desirable to ensure that the majority of neutrons have not scattered before detection, the neutron mean free path in which the instrument is operated must be considered. The mean free path is the average distance a particle will travel without interacting in a medium. For example, to assay irradiated fuels in wet storage, the front of the device must be placed within 7.12 cm of the fuel assembly

because water has a large cross section for neutron-proton elastic scattering. If it is possible to assay spent fuel in air, the device can be several meters away.

3.3. Optimization for Detecting (α , n) Neutrons

This section presents a procedure for optimizing the proposed neutron detector to perform precision neutron spectroscopy of spent fission reactor fuel to observe (α , n) reactions. This optimization does come at the cost of efficiency, which means fewer neutrons are detected. The variables controlling the energy resolution and efficiency, labeled in Figure 3.1, are the scattering angle (θ) and the distance (L) between the cells. A trade study is necessary to determine the best choice of L and θ to achieve high-resolution energy measurements while maintaining reasonable detector efficiency.

An analytical model is developed in 3.3.1 to determine the dependence of the energy resolution and detector efficiency on L and θ . This model is applied in 3.3.2 for the detection of 1.9-MeV neutrons produced from the interaction of 5.2-MeV α particles in UO_2 fuel. Limitations of this analysis are examined in 3.3.3.

3.3.1. Analytical Model of Neutron Detection Physics

Recall that the main mechanism behind scintillation detectors is neutron elastic scattering off hydrogen nuclei in the scintillator. Detection may also occur when a neutron scatters elastically off a carbon nucleus in the scintillator; however, the energy measurement will be of much lesser quality. The maximum ratio of the energy gained by a recoil nucleus (initially at rest) to the energy of the incident neutron in elastic scattering is given by (3.4).

$$\frac{E_r}{E_n} = \frac{4m_n m_r}{(m_n + m_r)^2} \quad (3.4)$$

This equation results in a ratio of 1.0 for hydrogen and 0.28 for carbon.

The total microscopic cross section for neutron reactions in these nuclei is dominated by elastic scattering. This cross section is roughly equal for hydrogen and carbon. The majority of detected neutrons in scintillation detectors, however, result from interactions with hydrogen. This is because recoil carbon nuclei are often not energetic enough to generate a sufficient light output to trigger the processing electronics.

The macroscopic cross section is calculated according to (3.5) for neutron elastic scattering in scintillation detectors of type i .

$$\epsilon_i = \sigma_H n_{i,H} + \sigma_C n_{i,C} \quad (3.5)$$

It accounts for the microscopic cross sections and the number density n of each of nuclei present. The probability that a neutron will scatter in detector i depends on the macroscopic cross section of the scintillator and is given by (3.6), where x is the detector thickness.

$$P_i = 1 - \exp[-x\epsilon_i] \quad (3.6)$$

The scintillators used in NSPECT and the proposed device are 1" right circular cylinders. This dimension will be used for x .

The relationship between the incident neutron energy, the neutron scattering angle, and the scattered neutron kinetic energy is shown in (3.7).

$$E_n = E_T \sec^2 \theta \quad (3.7)$$

The variance of the incident neutron energy in (3.8), which is related to the FWHM according to (3.9), was derived using (2.2) and (3.7).

$$\begin{aligned}
\sigma_n^2 &= \left(\frac{\partial E_n}{\partial t} \right)^2 \sigma_t^2 \\
&= \frac{8E_T^3}{mL^2} \sigma_t^2 \\
&= \frac{8}{mL^2} (E_n \cos^2 \theta)^3 \sigma_t^2
\end{aligned} \tag{3.8}$$

$$FWHM = 2\sigma_n \sqrt{2 \ln 2} \tag{3.9}$$

The derivation of (3.8) assumes perfect energy measurements in D1 and D2 to remove the correlation between the ToF resolution and the energy resolution in D1 and D2. The resulting equation in (3.8) also demonstrates how the incident neutron energy resolution can be improved simply by increasing L or θ .

Increasing L decreases the solid angle subtended by D2 for neutrons scattering in D1. This reduces the instrument's *efficiency* and thus limits the extent to which the energy resolution may be optimized. Detector efficiency is the ratio of the number of particles detected to the number of particles available for detection. The efficiency can also be thought of as the probability of a particle scattering from D1 into D2 and then scattering again in D2, assuming the particle is detected when it scatters.

Neutron-proton elastic scattering is isotropic in the center-of-mass reference frame. The efficiency of the proposed instrument in the center-of-mass reference frame of the neutron-proton system is found using (3.10).

$$\varepsilon = \left[\left(\frac{d\sigma'}{d\Omega'} d\Omega'_2 \right) \left(\frac{n_{1,H}}{\epsilon_1} P_1 \right) \right] \left[\sigma_H \frac{n_{2,H}}{\epsilon_2} P_2 \right] \tag{3.10}$$

The variables P and ϵ are the probability and macroscopic cross sections from (3.6) and (3.5), respectively. The number density of hydrogen is 5.21×10^{22} atoms/cm² for D1 and

4.65×10^{22} atoms/cm² for D2 [6, 7]. The number density of carbon is 4.74×10^{22} atoms/cm² for D1 and 5.43×10^{22} atoms/cm² for D2 [6, 7].

The differential cross section is used in (3.10) to determine the probability of neutron scattering from D1 to D2 because the scatter is restricted to the solid angle subtended by D2. The differential cross section in (3.10) may be replaced with (3.11) because the neutrons scatter isotropically in the center-of-mass frame.

$$\frac{d\sigma'}{d\Omega'} = \frac{\sigma_H}{4\pi} \quad (3.11)$$

Also, notice how this efficiency does not account for detection resulting from neutron elastic scattering with carbon nuclei. This is because, according to (3.4), interactions with carbon nuclei do not result in sufficient light output for detection. They do, however, affect the number of neutrons available for detection which is why the neutron cross section for carbon is included in (3.5).

The detector efficiency must be transformed to the laboratory frame because that is the frame in which measurements are made. The total cross-section for neutron-proton elastic scattering is independent of the reference frame. This principle is applied to obtain (3.12), which describes the relationship between the differential cross sections in each frame.

$$\frac{d\sigma}{d\Omega} d\Omega_2 = \frac{d\sigma'}{d\Omega'} d\Omega'_2 \quad (3.12)$$

The prime symbol in (3.11) and (3.12) denotes variables in the center-of-mass frame.

Expressing (3.12) in terms of the scatter angle θ results in (3.13).

$$\frac{d\sigma}{d\Omega} = \frac{d\sigma'}{d\Omega'} \left(\frac{\sin \theta' d\theta'}{\sin \theta d\theta} \right) = \frac{d\sigma'}{d\Omega'} (4 \cos \theta) \quad (3.13)$$

Changing the reference frame for the solid angle defined by D2, shown in (3.14), required combining (3.12) and (3.13).

$$d\Omega'_2 = 4 \cos \theta d\Omega_2 \quad (3.14)$$

The solid angle subtended by D2 in the laboratory frame is estimated in (3.15) as the solid angle of a circle seen by a point source of scattered neutrons in D1 (Figure 3.3).

$$\begin{aligned} d\Omega_2 &= \int_0^{2\pi} d\varphi \int_0^{\beta} \sin \vartheta d\vartheta \\ &= 2\pi \left(1 - \frac{L}{\sqrt{L^2 + R^2}} \right) \end{aligned} \quad (3.15)$$

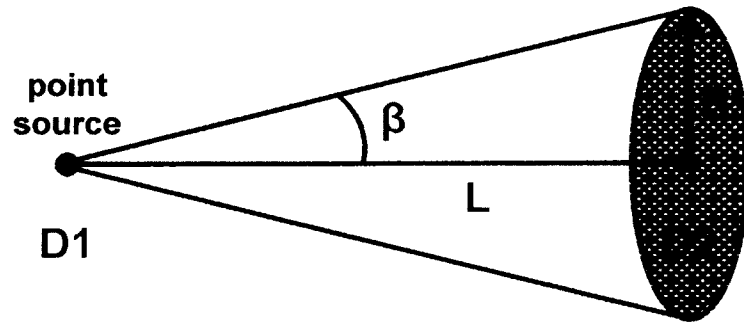


Figure 3.3. An illustration for approximating the solid angle of D2 in the laboratory frame. Neutrons are assumed to scatter at the center of D1. The radius R of each cell is 2.54 cm.

$$\varepsilon = \sigma_H^2 \left[2 \cos \theta \left(1 - \frac{L}{\sqrt{L^2 + R^2}} \right) \left(\frac{n_{1,H}}{\epsilon_1} P_1 \right) \right] \left[\frac{n_{2,H}}{\epsilon_2} P_2 \right] \quad (3.16)$$

Combining (3.10), (3.13), (3.14), and (3.15) results in (3.16) – the detector efficiency in the laboratory frame.

3.3.2. Procedure for Optimization

Alpha particles emitted from plutonium in the reactor fuel have an average energy of 5.2 MeV and are reported to produce neutrons with an average energy of 1.9 MeV in a thick target of oxygen [8]. At this incident neutron energy, the total microscopic cross section is 2.6 barns for hydrogen and 1.6 barns for carbon [1]. A procedure is outlined in this section to perform a trade study analysis with results from (3.8) and (3.16) that may be used with any incident neutron energy.

The 1.9-MeV incident neutron energy was selected to provide a realistic example for optimizing the energy resolution and efficiency of the proposed detector. Alpha particles in UO₂ fuel are not monoenergetic because there are numerous fission and decay products that emit alphas. This was also considered when selecting 1.9-MeV neutrons. Optimization at a lower energy makes it possible to detect more energetic neutrons without changing L or θ (energy resolution improves as energy increases). Finally, 1.9-MeV neutrons present a worst-case scenario because their close proximity to the fission spectrum peak will make them difficult to identify.

Possible values for L and θ are identified in Figure 3.4 where the energy resolution is about 0.2 MeV FWHM. This is the incident neutron energy resolution for 1.9-MeV neutrons measured with NSEPCT. From this figure it is clear that lower values of L and higher values of θ are preferable. In particular, choosing L and θ to be 5 cm and 55°, respectively, produces the best efficiency for the desired energy resolution.

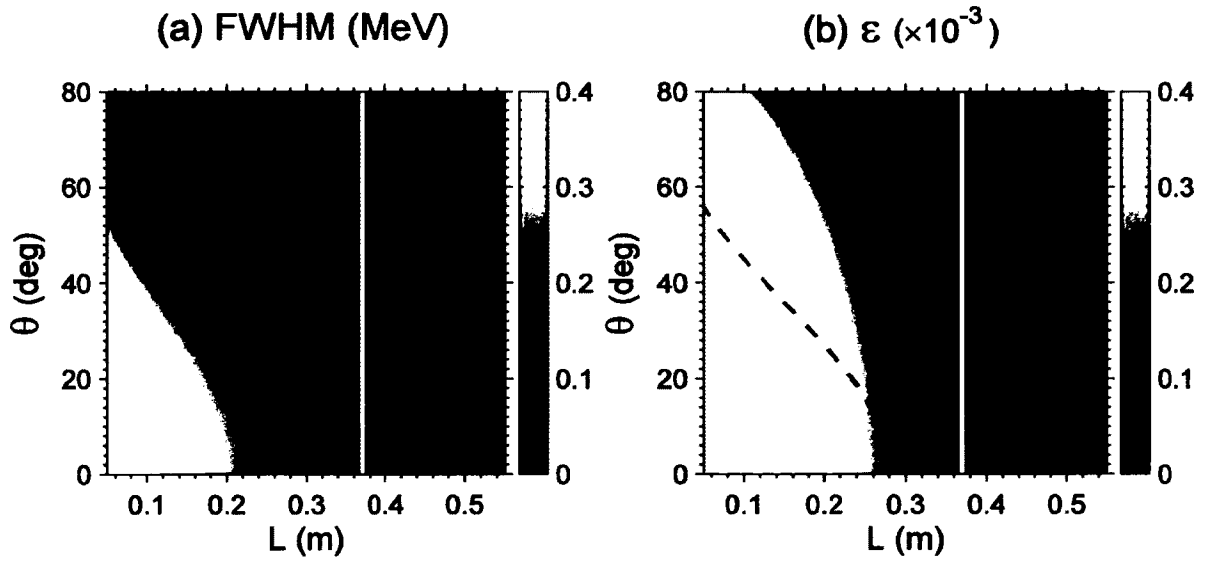


Figure 3.4. Equations (3.8) and (3.16) are plotted in (a) and (b), respectively, as a function of L and θ . The dashed green line marks a neutron energy resolution of 0.2 MeV FWHM. The solid white line is drawn at the D1/D2 cell separation in NSPECT.

3.3.3. Analysis Limitations

The results from Figure 3.4 provide choices for L and θ that can be used to perform a trade study in the laboratory. Testing the detector performance might involve placing the cells at a fixed separation while varying θ . This would provide a range of acceptable values for θ at a given L . A range in θ may be necessary for a large neutron source like spent reactor fuel where the scatter angle is not easily controlled.

The factors described below are not accounted for in the derivation of (3.8) and (3.16). Including these factors will limit the choices for optimization parameters. A numerical analysis would be required because it would no longer be possible to create an analytical model.

- Energy measurements in D1 and D2 are assumed to be perfect. This made it possible to ignore energy dependences in the ToF resolution. Accounting for this requires consideration of the correlation between the ToF resolution and the energy

resolution in D1 and D2. Choices of L and Θ in Figure 3.4 must increase to compensate, which should provide better agreement with the cell separation in NSPECT.

- Poor energy resolution in D1 at low scatter angles and in D2 at large scatter angles will restrict choices of Θ to a smaller range. Thresholds on energy measurements in D1 and D2 will place similar restrictions on Θ .
- ToF resolution will increase the minimum choice of L . If the cell separation is too small the ToF for γ rays and neutrons will differ by less than the ToF resolution. This would make events indistinguishable.
- In (3.6), x is assumed to be the same for all neutrons entering D1 or D2. In reality, x depends on the angle between the incident neutron velocity vector and the normal vector relative to the point of entry at the detector surface. It also depends on the size and shape of the detector. Integration over the detector volume is required, which is quite complicated when the source is not isotropic and point-like.
- In (3.15), the solid angle subtended by D2 is estimated as that of a circular disk seen by an isotropic point-source of neutrons located on-axis. A proper treatment of this calculation requires integration over the volume of D1. This integration involves Bessel functions and cannot be solved analytically [9]. The source of neutrons incident on D1 is also assumed to be point-like and would require similar treatment.
- In (3.10) and (3.16), it is assumed that neutrons do not interact with passive material and that they deposit sufficient energy for detection in both D1 and D2. Numerical simulations are required to account for these effects.

3.4. Comparing Design to NSPECT

Testing was performed in the laboratory with one plastic detector and one stilbene detector taken from NSPECT. The cells were placed 30 cm apart and connected to standard laboratory electronics rather than the custom NSPECT processing electronics. A prototype of the proposed instrument in Figure 3.1 would be similar to this two-cell test. Data were acquired for a ^{60}Co source placed between the cells as described in Section 2.4.

The ^{60}Co energy spectrum and detector energy resolution obtained with the two-cell setup are provided in Figure 3.5. For comparison, the ^{60}Co energy spectrum measured with NSPECT is shown in Figure 3.6. In both figures, the stilbene cells appear to have a slightly better resolution than the plastic cells. The γ -ray energy resolution for NSPECT, determined mainly from D3, is 20% at 662 keV [2]. The two-cell setup has an energy resolution of approximately 13% at 662 keV, which is much improved from NSPECT.

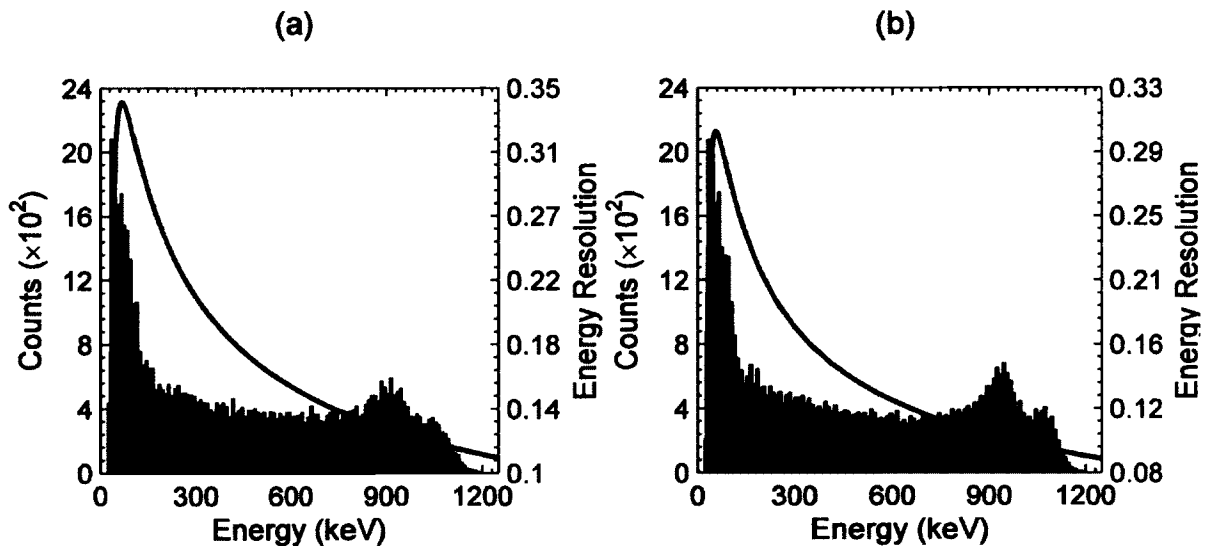


Figure 3.5. Co-60 energy spectrum and energy resolution measured with (a) D1 and (b) D2 cells in the two-cell setup.

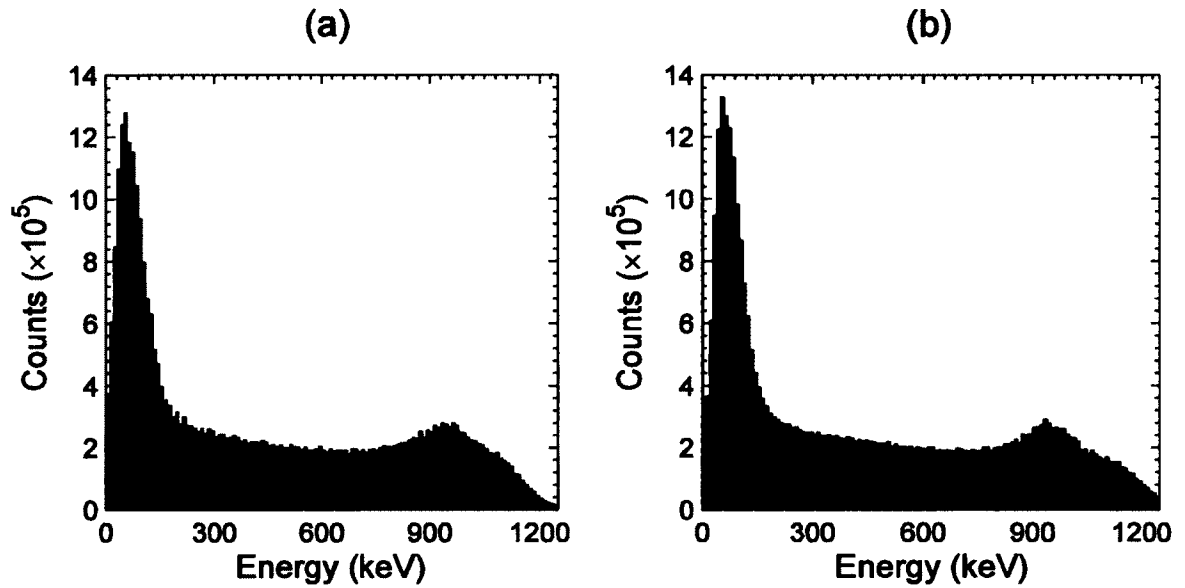


Figure 3.6. Co-60 energy spectrum measured with (a) D1 and (b) D2 layers in NSPECT. The energy resolution function for each detection layer has yet to be determined.

Differences in energy resolution between NSPECT and the two-cell setup are likely a result of the electronics used to collect data. It could also be caused by the number of cells used because NSPECT has twenty-five times more than the engineering model. The number of cells affects the energy resolution because each cell introduces an uncertainty as a result of the individual energy calibrations from ADC channel to keV.

The ToF resolution is approximately the same for the two instruments. In the two-cell setup, the ToF resolution is 0.635 ns FWHM, where the ⁶⁰Co data were limited to recorded energies between 200 keV and 800 keV. As discussed in Section 2.7, this avoids the low-energy peak and the Compton edge. The ToF resolution for NSPECT, using the same energy restrictions, is 0.587 ns FWHM with just D1_{C13} and D2_{C13} and 0.604 ns FWHM with all cells in D1 and D2.

3.5. Final Remarks

A design for neutron detection based on the NSPECT instrument was proposed in this chapter. Optimizing such a device to perform precision neutron spectroscopy of spent fuel for the observation of neutrons from (α , n) reactions was discussed in detail. The information gathered from the assay of spent fuel can be interpreted and used for various applications. Examples include determining the extent to which neutron poisons have developed in the fuel assemblies and measuring the activity of spent fuel to assist in storage and transportation decisions.

The proposed design is adaptable for contamination monitoring in a nuclear power plant. It can be operated by a single technician at greater distances to reduce the exposure during inspection. Information gathered by this instrument may also be useful for predicting the behavior of a reactor in the event of an accident. The versatility of the two-cell design could be improved with additional scintillation detectors, the calibration of which would require some automation. The cells could be exchanged to enable the detection of γ rays.

The ToF system directly affects optimization of the energy resolution for neutron detection. A procedure has been discussed to obtain a neutron energy resolution of 0.2 MeV FWHM for identifying neutrons produced by (α , n) reactions. This procedure can be utilized to adapt this instrument design for other applications simply by balancing the energy resolution and detector efficiency as desired.

4. CONCLUSION

The NSPECT ToF system as it stands presently is fully calibrated with a resolution of 0.72 ns FWHM. Automated software may be developed from existing code to test current ToF corrections described in Chapter 2 and to fix any that may have changed. The necessary features for creating this software have been provided in Section 0.

A design is proposed in Chapter 3 for a device based on the NSPECT neutron detection system. Optimizing this instrument is discussed for detecting 1.9 MeV neutrons from (α , n) reactions with 0.2 MeV FWHM, which is the incident neutron energy resolution for 1.9 MeV neutrons measured with NSEPCT. Good ToF resolution is required for neutron spectroscopy with NSPECT and this device because of its key role in incident neutron energy measurements. Calibration and maintenance of the ToF system is discussed in detail in Chapter 2.

Optimization of the proposed neutron detector for a particular measurement involves a trade-off between efficiency and energy resolution. These values are optimized by adjusting the separation between cells and controlling the angle of incident neutrons. A trade study is required to assess the accuracy of the analytical estimates in Section 3.3 and determine the extent to which the scatter angle can be controlled.

LIST OF REFERENCES

- [1] V. McLane, C. L. Dunford and P. F. Rose, *Neutron Cross Sections*, vol. 2, San Diego, CA: Academic Press, Inc., 1988.
- [2] A. C. Madden, P. F. Blosser, D. Fourgette, L. Larocque, J. Legere, M. Lewis, M. L. McConnell, M. Rousseau and J. M. Ryan, "An Imaging Neutron/Gamma-Ray Spectrometer," in *Chemical, Biological, Radiological, Nuclear, and Explosives (CBRNE) Sensing XIV*, Baltimore, MD, 2013.
- [3] IAEA, "Power Reactor Information System (PRIS)," 2013. [Online]. Available: <http://www.iaea.org/pris/>. [Accessed May 2013].
- [4] K. S. Krane, *Introductory Nuclear Physics*, New York, NY: John Wiley & Sons, 1988.
- [5] T. Jevremovic, *Nuclear Principles in Engineering*, New York, NY: Springer Science & Business Media, Inc., 2005.
- [6] Saint-Gobain, "Saint-Gobain Crystals - Plastic Scintillators," 2013. [Online]. Available: <http://www.detectors.saint-gobain.com/Plastic-Scintillator.aspx>. [Accessed February 2013].
- [7] W. R. Leo, *Techniques for Nuclear and Particle Physics Experiments: A How-to Approach*, 2 ed., New York, NY: Springer-Verlag, 1994.
- [8] D. Reilly, N. Ensslin, H. J. Smith and S. Kreiner, *Passive Nondestructive Assay of Nuclear Materials*, Los Alamos, NM: United States Nuclear Regulatory Commission, 1991.
- [9] G. F. Knoll, *Radiation Detection and Measurement*, 4 ed., Hoboken, NJ: John Wiley & Sons, 2010.
- [10] J. M. Ryan, C. Bancroft, P. Blosser, D. Fourgette, L. Larocque, J. Legere, A. Madden, M. L. McConnell, J. Pavlich, G. Ritter, G. Wassick and M. Rousseau, "An Imaging Neutron/Gamma-Ray Spectrometer," in *Penetrating Radiation Systems and Applications XIII*, San Diego, CA, 2012.

APPENDIX

This chapter examines the γ -ray events excluded in Section 2.7. These events are not part of the Compton continuum, which should be the dominant feature in the energy spectrum for a γ -ray source measured by a low-density scintillation detector. Events with energies above the Compton edge may be caused by random coincidences. The observed low-energy peak is likely the result of γ rays scattering from passive material into the scintillators.

The energy spectra for the ^{60}Co calibration data are provided in Figure A.1. Data obtained from a ^{137}Cs source, placed in front of NSPECT, are presented in Figure A.2. These figures demonstrate the large peak below 0.2 MeV that was present in both energy spectra. This peak also appeared in energy histograms of the ^{22}Na data used in Section 2.5.

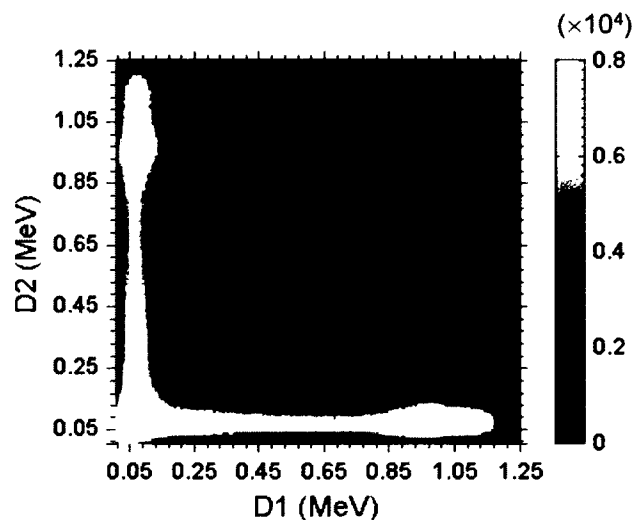


Figure A.1. Density plot of ^{60}Co energy spectra measured by the D1 and D2 detector planes. The ^{60}Co data presented are the same calibration data used in Chapter 2.

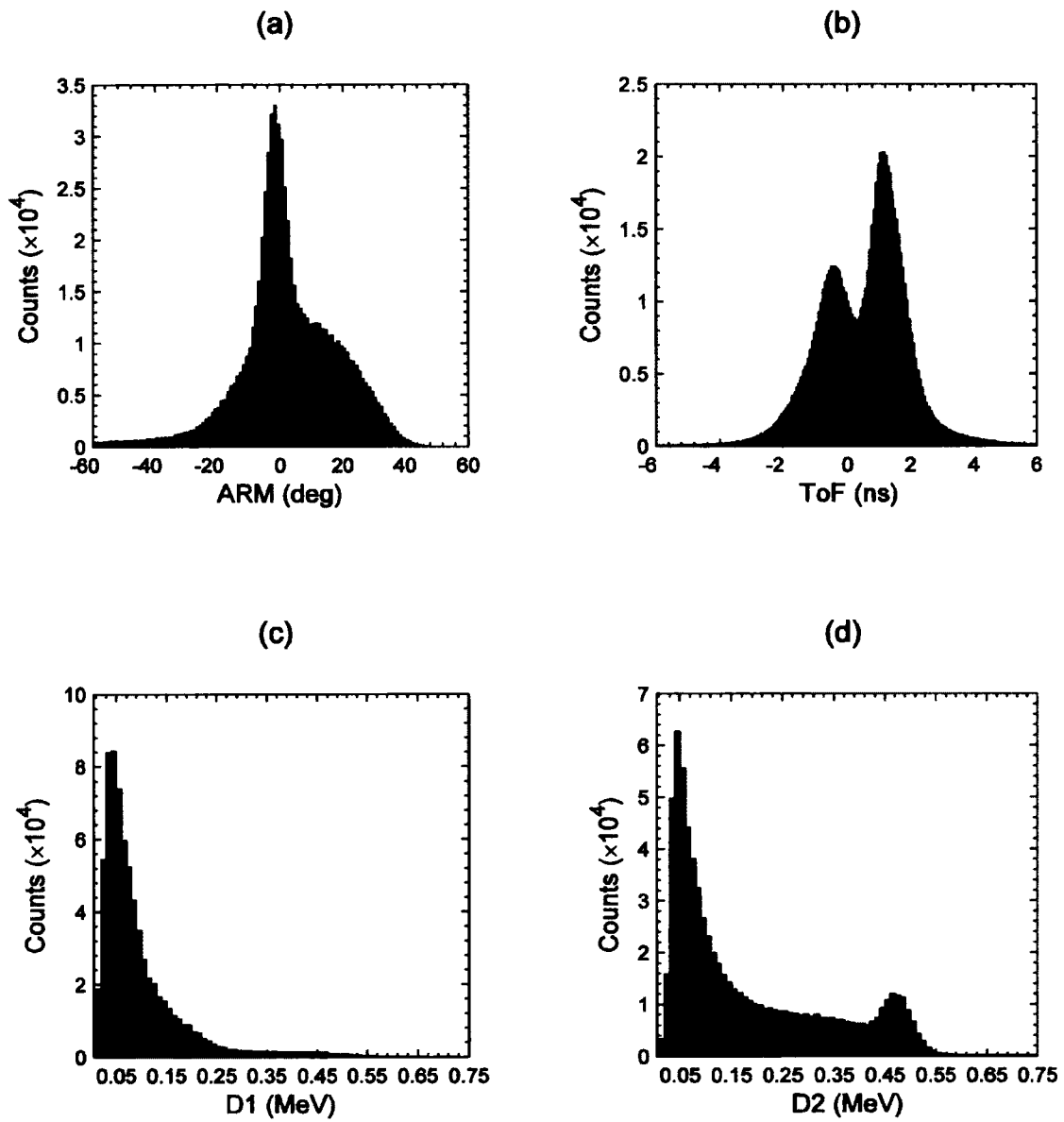


Figure A.2. Measurements of (a) the ARM, (b) the ToF, (c) energy in D1, and (c) energy in D2 from a ^{137}Cs source placed on-axis and 2 m in front of NSPECT. (continued)

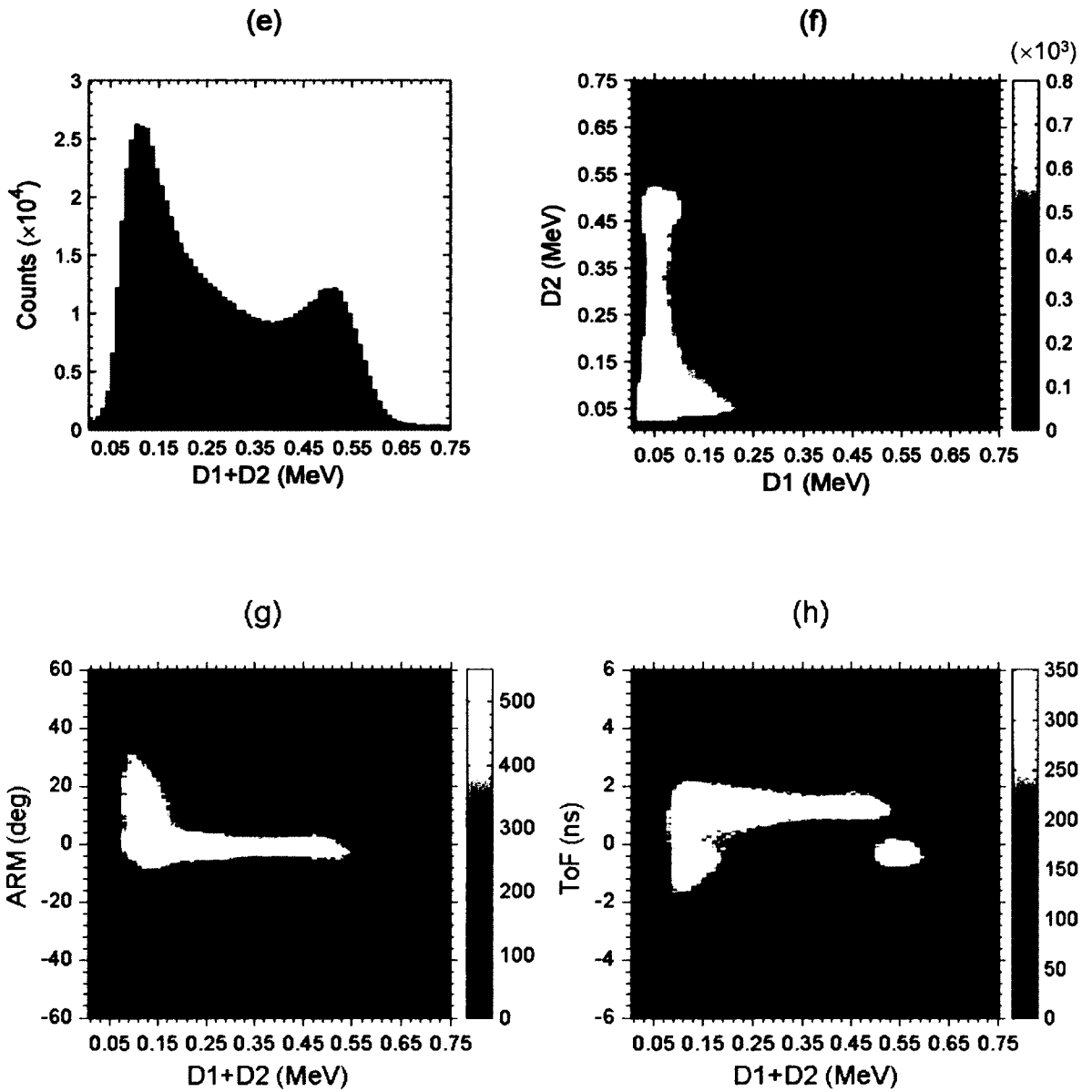


Figure A.2 (continued). (e) A histogram of the net energy measured in D1 and D2. (f) A density plot of the D1 and D2 energies. A density plot of (g) the ARM and (h) the ToF versus the net energy measured in D1 and D2.

Regardless of their origin, it is expected that the majority of events in the low-energy peak did not contribute to accurate ToF measurements. These events in the ^{137}Cs data are also likely to produce poor imaging results. Applying restrictions on the ToF and angular resolution measure (ARM) of the ^{137}Cs data should significantly reduce the low-energy peak and remove events observed above the Compton edge. This would confirm the above suspicions regarding the source of these events and validate their exclusion from analysis.

A.1. *Data Characterization*

There are several filters in the NSPECT hardware and software for sorting recorded events. Good events are defined as recorded events that allow the imaging software to determine the source location. Examples of bad events include the detection of two unrelated particles and the detection of a particle originating from the source that interacts in passive material before detection. The hardware contains a 50-ns requirement for coincidence between D1 and D2, a 5-ns requirement for coincidence between D2 (or D1) and D3, and a 50-keV energy threshold in each detector layer to prevent the recording of electronic noise [10]. The software for NSPECT was carefully developed to separate good events from bad using three parameters that characterize each event: PSD, ToF, and ARM.

The data examined here consist entirely of events from γ -ray sources, which means PSD measurements will not be used. Because double-scatters from single γ rays are assumed in ARM calculations, they are useless for the ^{60}Co data but will be applied to the ^{137}Cs data. Restrictions on the ToF measurement are sufficient for removing many of

the random coincidences observed above the Compton edge in both sets of data but are not effective in reducing the low-energy peak.

A.1.1. Angular Resolution Measure

The ARM is an important parameter for an imaging telescope such as NSPECT. It is defined as the difference between the scatter angle calculated from the Compton energy equation for γ rays, or elastic scattering for neutrons, and the scatter angle calculated from the known geometry of NSPECT (See Figure 2.2). In the NSPECT imaging software, the FWHM of the ARM distribution represents the uncertainty in the source location. The imaging software uses the ARM to select data around a source location on the image plane to construct an energy spectrum. The restricted energy spectrum is expected to have fewer anomalies than the original spectrum. The ARM for NSPECT was determined to be about 10° FWHM for γ rays [2].

The nature of γ -ray interactions between D1 and D2 will result in meaningless ARM calculations for unknown sources because double Compton scatters prevent the measurement of incident γ -ray energies. In other words, a γ ray will most likely escape D1 and D2 before being fully absorbed. Detection of two quasi-simultaneous calibration γ rays, essential for Chapter 2, will also result in meaningless ARM calculations. With a source placed in front of NSPECT, the ARM may be calculated. A monoenergetic γ -ray source (^{137}Cs) was placed on-axis and in front of NSPECT to investigate the anomalous features present in the energy spectra of γ -ray sources, such as the ^{60}Co calibration data, measured by D1 and D2.

A.1.2. Compton Scattering

The scintillators in D1 and D2 were selected for their large neutron elastic scattering cross sections, but they also have cross sections for Compton scattering. Because of their low densities, D1 and D2 have small cross sections for fully absorbing γ rays. This means that the majority of γ rays detected in D1 and D2 interacted via Compton scattering.

Backscatter peaks and photopeaks, which result from the complete absorption of a γ ray, are not present in any energy spectra measured by D1 or D2. This is due to the nature of the γ -ray interactions in these cells and the double-scatter coincidence requirements. Even under ideal conditions, the energy available to the second detector will be less than the incident γ -ray energy because the γ ray has already lost some of its energy in the first detector. The sum of the energies deposited in the two detectors should, of course, not exceed the incident γ -ray energy.

$$\frac{1}{E'} - \frac{1}{E} = \frac{1}{E_0} (1 - \cos \theta) \quad (\text{A.1})$$

The Compton energy equation, as shown in (A.1), may be solved for the scatter angle if the incident γ -ray energy (E) and the scattered γ -ray energy (E') are known. The electron rest-mass was taken to be 511 keV. Backscattered photons from ^{60}Co ($90^\circ < \theta < 270^\circ$) may deposit up to 1.12 MeV in D2. This corresponds to the Compton edge, which is ideally the highest energy that D1 and D2 can measure for ^{60}Co γ rays. It may be possible to measure energies above the Compton edge as a result of γ -ray absorption, but there should not be many events where this happens.

Forward Scatter				Backward Scatter			
Θ (°)	D1 (keV)	D2 (keV)	D1+D2 (keV)	Θ (°)	D1 (keV)	D2 (keV)	D1+D2 (keV)
59.64	258.30	246.94	505.24	132.09	94.18	452.46	546.64
0.00	0.00	661.7	661.7	180.00	77.25	477.34	554.58

Figure A.3. Compton scatter results for ^{137}Cs .

The energies that would ideally be measured for all possible double-scatter cell combinations were determined for the ^{137}Cs source using Figure A.3. For these calculations the following assumptions were made: (1) Scattering takes place at the center of each scintillator, (2) the energy lost by a γ ray is fully collected by the detecting cell, (3) γ rays deposit the maximum possible energy ($\Theta = 180^\circ$) when scattering in the second detector, and (4) γ rays do not interact with any passive material before detection. The resulting extrema are presented in Figure A.3 for forward and backward scattering. Applying the energy resolution to these values and comparing them to Figure A.2 makes it clear that the energy spectra contain features that are not part of the Compton continuum.

Forward scattering γ rays with the minimum scatter angle should fail to meet coincidence requirements because no energy is lost in D1. In reality, double-scatter γ -ray events can have 0° geometric scatter angles, but (A.1) will have a non-zero result. The ARM is used to account for this discrepancy. If it were possible to pinpoint the location of the scattering interaction within a cell, these events would have the same geometric and Compton scatter angles and the ARM would be zero. Of course, this is assuming all cells take perfect energy measurements because (A.1) will be affected by the energy resolution.

A.2. Analysis & Results

The peaks in the ToF representing forward and backward scattered events are visible in Figure A.2, but they overlap significantly near 0 ns resulting in some distortion of the maximum location of each peak. This overlap makes the separation of forward and backward scattered events quite difficult. Consequently, the ARM was calculated assuming all events were forward scatters.

The data shown in Figure A.4 was restricted to ToF values between 1.25 ns and 1.85 ns (a range of $\sim 2\sigma_t$). The majority of events in this figure should be forward scatters because overlap with the backscatter peak in the ToF spectrume should be quite small. The ARM distribution is qualitatively Gaussian in shape and centered at zero degrees with a FWHM of 9° .

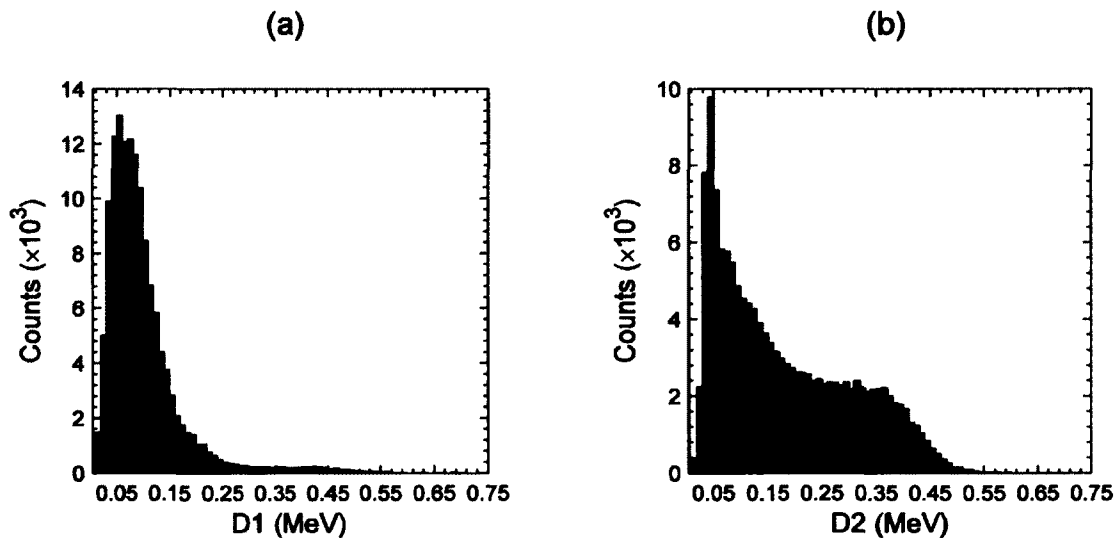


Figure A.4. Isolating the forward scatter peak of the ^{137}Cs data ($1.25 \text{ ns} \leq \text{ToF} \leq 1.86 \text{ ns}$). Measurements of (a) D1 energy and (b) D2 Energy. (continued)

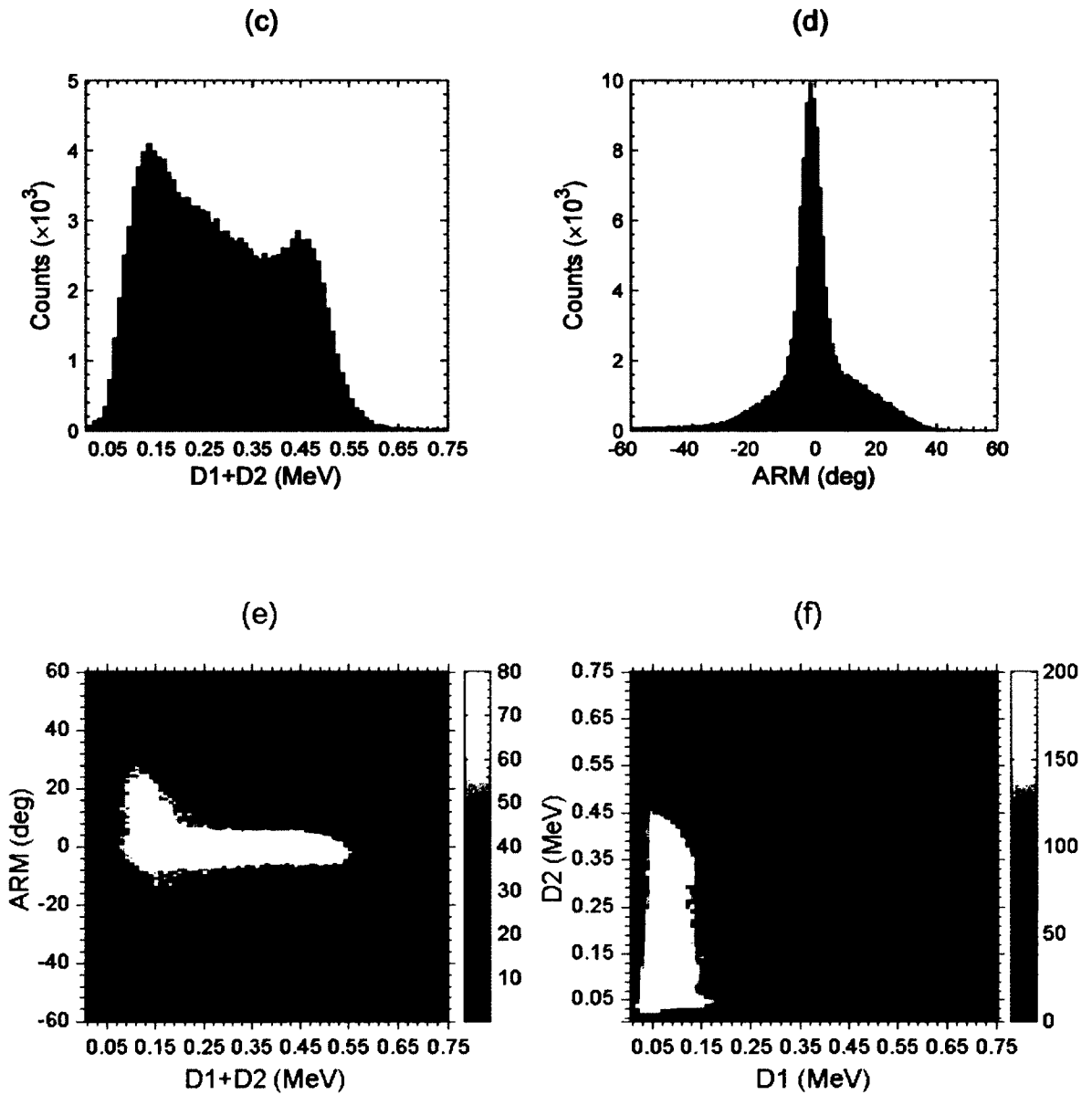


Figure A.4 (continued). (c) A histogram of the net energy measured in D1 and D2. (d) The ARM distribution. A density plot of (e) the ARM versus the net energy measured in D1 and D2 and (f) the D1 and D2 energies.

Similarly, in Figure A.5, the ToF was restricted to values between -1.85 ns and -1.25 ns. The majority of these events should be backward scatters. The ARM distribution is much broader and no longer centered at zero degrees as it was with forward scattering. This was expected because all events were assumed to be forward scatters.

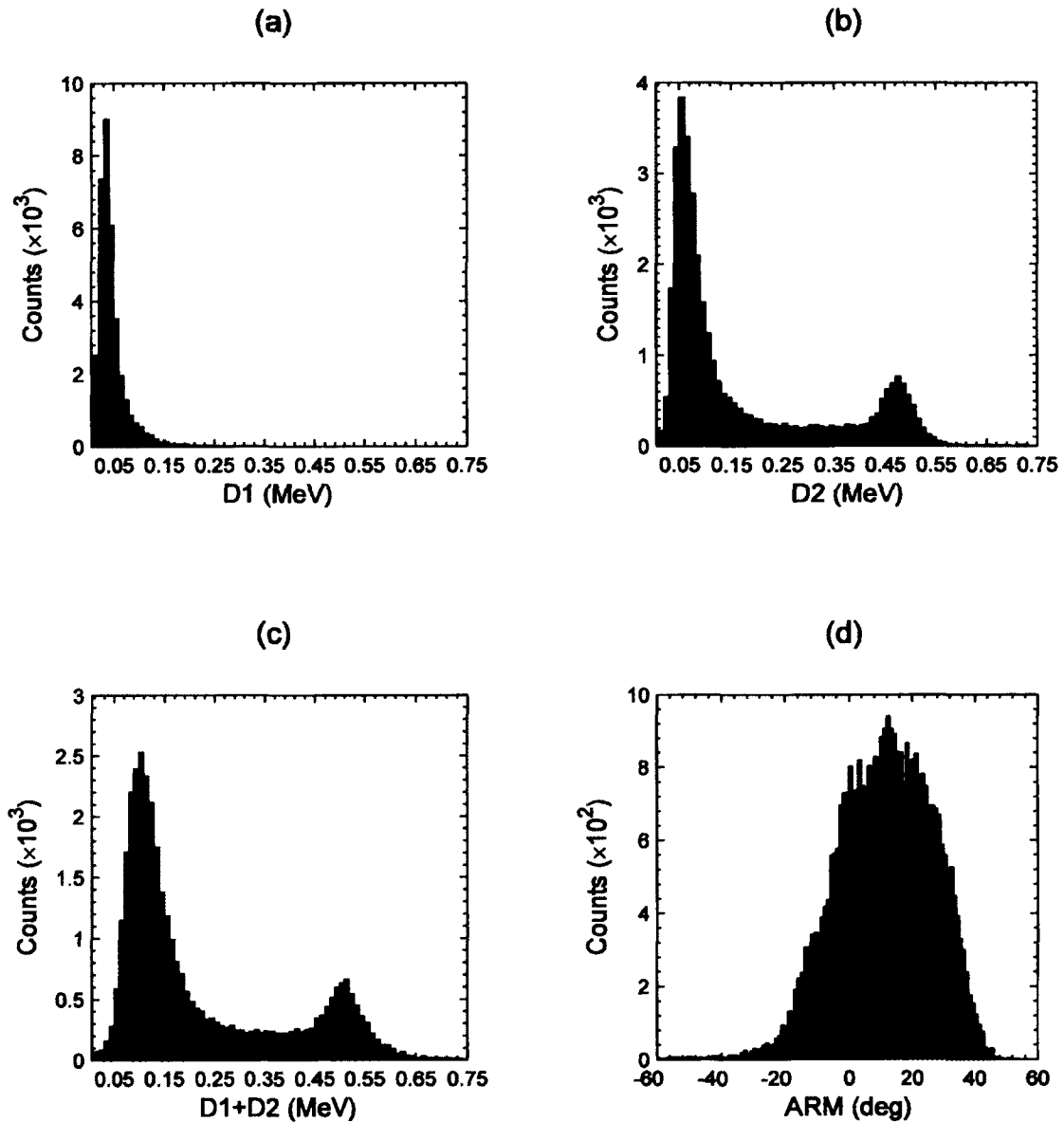


Figure A.5. Isolating the backward scatter peak of the ^{137}Cs data (-1.86 ns \leq ToF ≤ -1.25 ns). Measurements of (a) D1 energy, (b) D2 energy, (c) the net energy in D1 and D2, and (d) the ARM distribution. (continued)

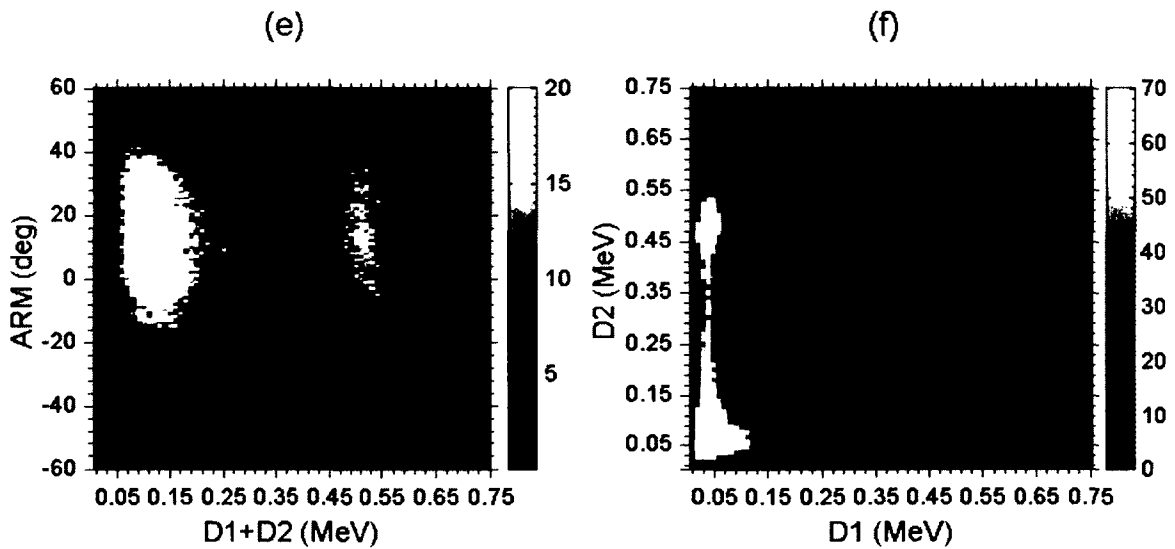


Figure A.5 (continued). A density plot of (e) the ARM versus the net energy measured in D1 and D2 and (f) the D1 and D2 energies

The forward scatter data from Figure A.4 are further limited to ARM values between $\pm 5^\circ$ (\pm HWHM) and is shown in Figure A.6. This was not done with the backward scatter data because little would be revealed.

For comparison, the same ^{137}Cs data are shown in Figure A.7 but with double-scatter events between D2 and D3 rather than D1 and D2. Notice how the anomalous peak below 0.2 MeV is absent from the energy spectra in this figure. Suppression of this peak may be due to the large γ -ray absorption cross section of D3. The ARM distribution has a FWHM of 10° .

The ToF measurement is not useful for the γ -ray detection layers because all γ rays travel at the speed of light. Consequently, the ToF has not been calibrated for these layers and ToF cuts cannot be made on the data in Figure A.7. The data are restricted to ARM values between $\pm 5^\circ$ and are shown in Figure A.8.

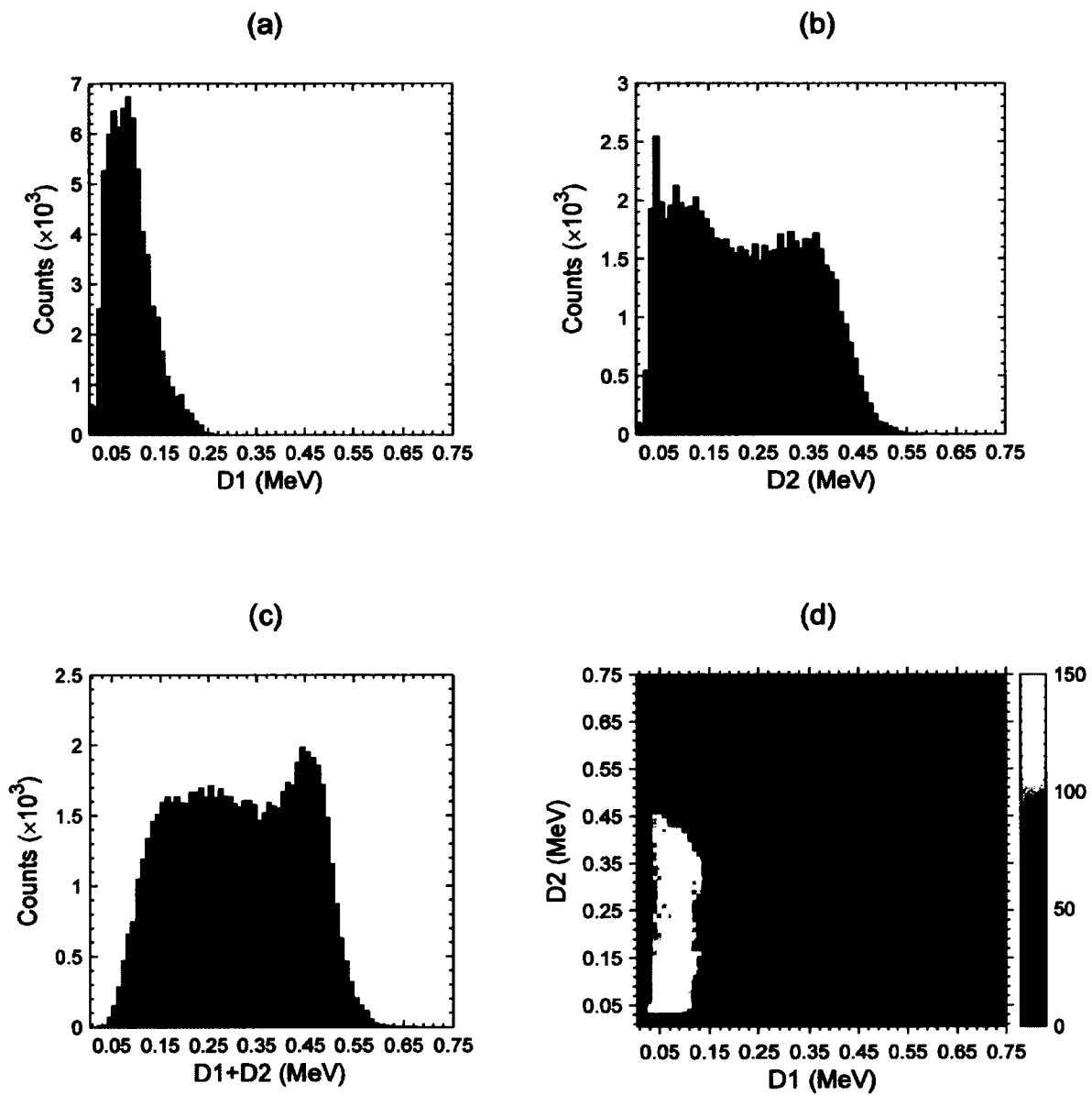


Figure A.6. Restricting the forward scatter peak data to $\pm 5^\circ$ ARM measurements. Histograms of (a) D1 energy, (b) D2 energy, and (c) the net energy in D1 and D2. (d) A density plot of the D1 and D2 energies.

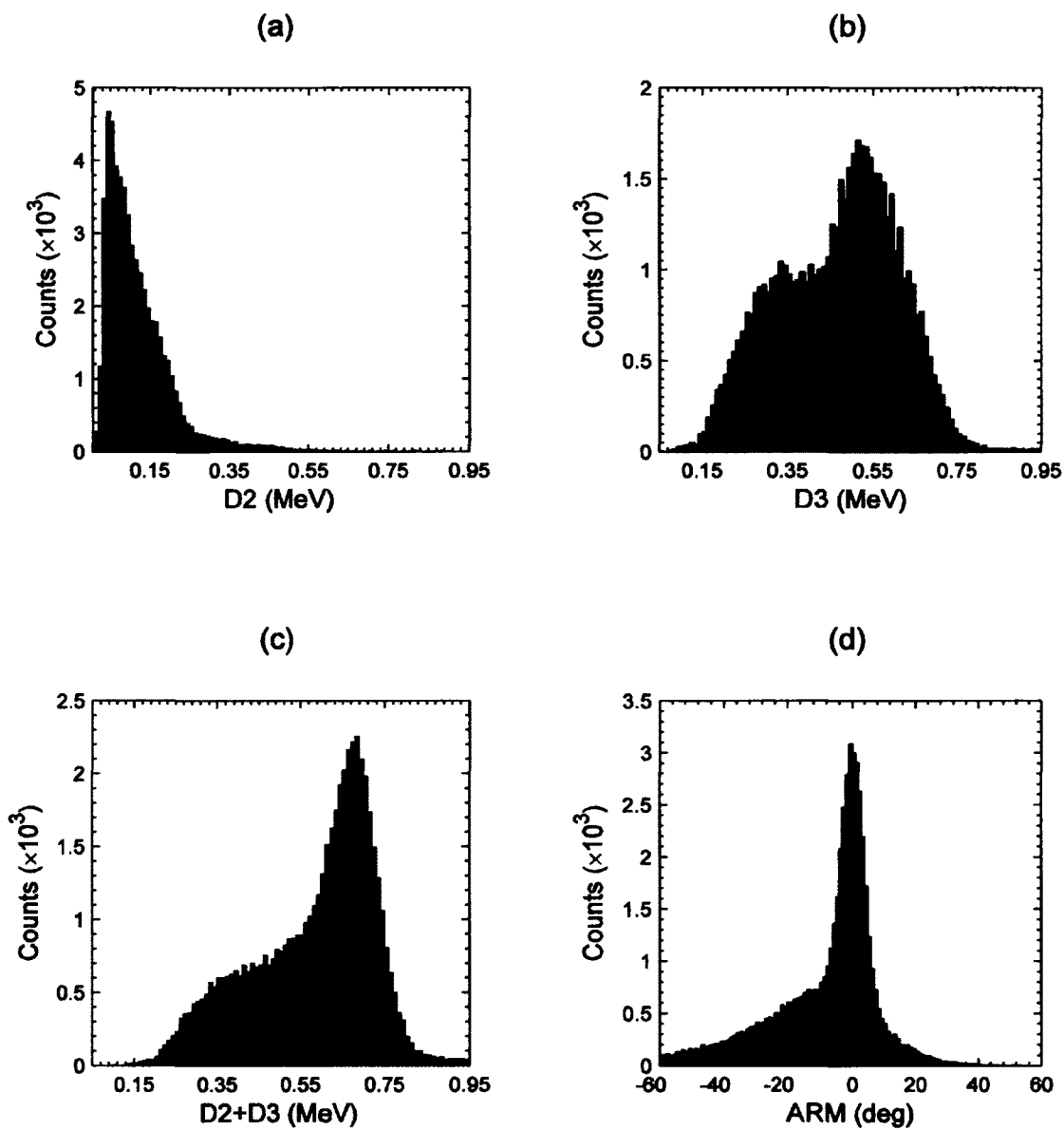


Figure A.7. The same ^{137}Cs data with measurements from the D2 and D3 detector planes. Measurements of (a) D2 energy, (b) D3 energy, (c) the net energy in D2 and D3, and (d) the ARM distribution. (continued)

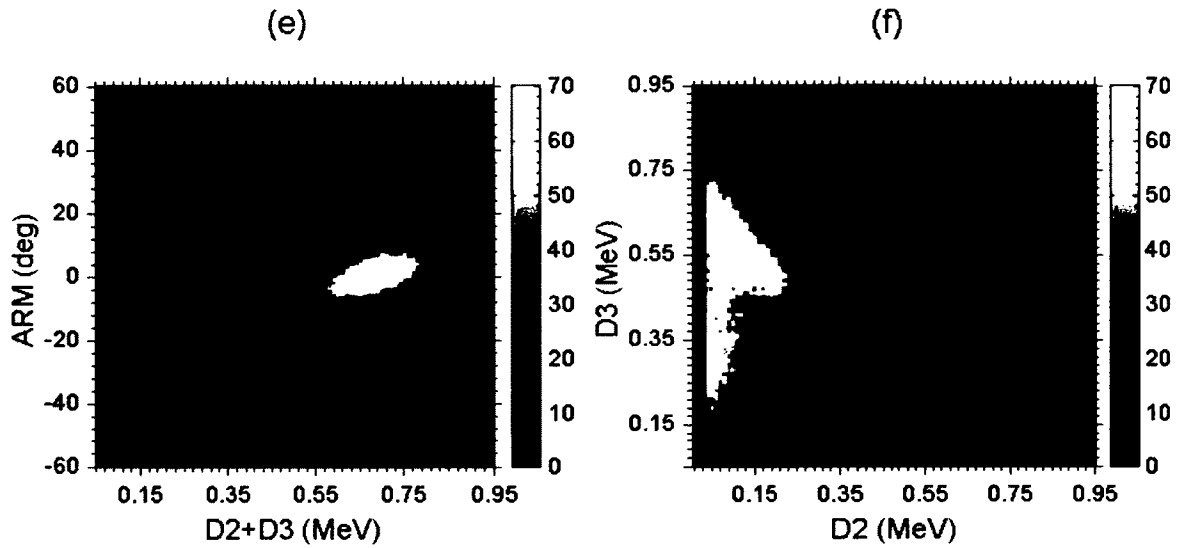


Figure A.7 (continued). A density plot of (e) the ARM versus the net energy measured in D2 and D3 and (f) the D2 and D3 energies

A.3. Discussion

The ToF cuts used in Figure A.4 and Figure A.5 reduce the number of events with recorded energies above the Compton edge, as do the ARM cuts used in Figure A.6 and Figure A.8. This confirms that the majority of these events are a result of random coincidence, where two γ rays are detected within the allowed coincidence window.

The low-energy peak in the forward scatter data is significantly decreased after the ARM cut shown in Figure A.6, revealing the expected Compton continuum. Comparing Figure A.4 and Figure A.5, the low-energy peak is also more prominent for backscatters than forward scatters. These results confirm that the majority of events in the low-energy peak do not provide meaningful information regarding the source characteristics. The figures above show that these events skew the energy spectra, ToF spectra, and ARM distribution.

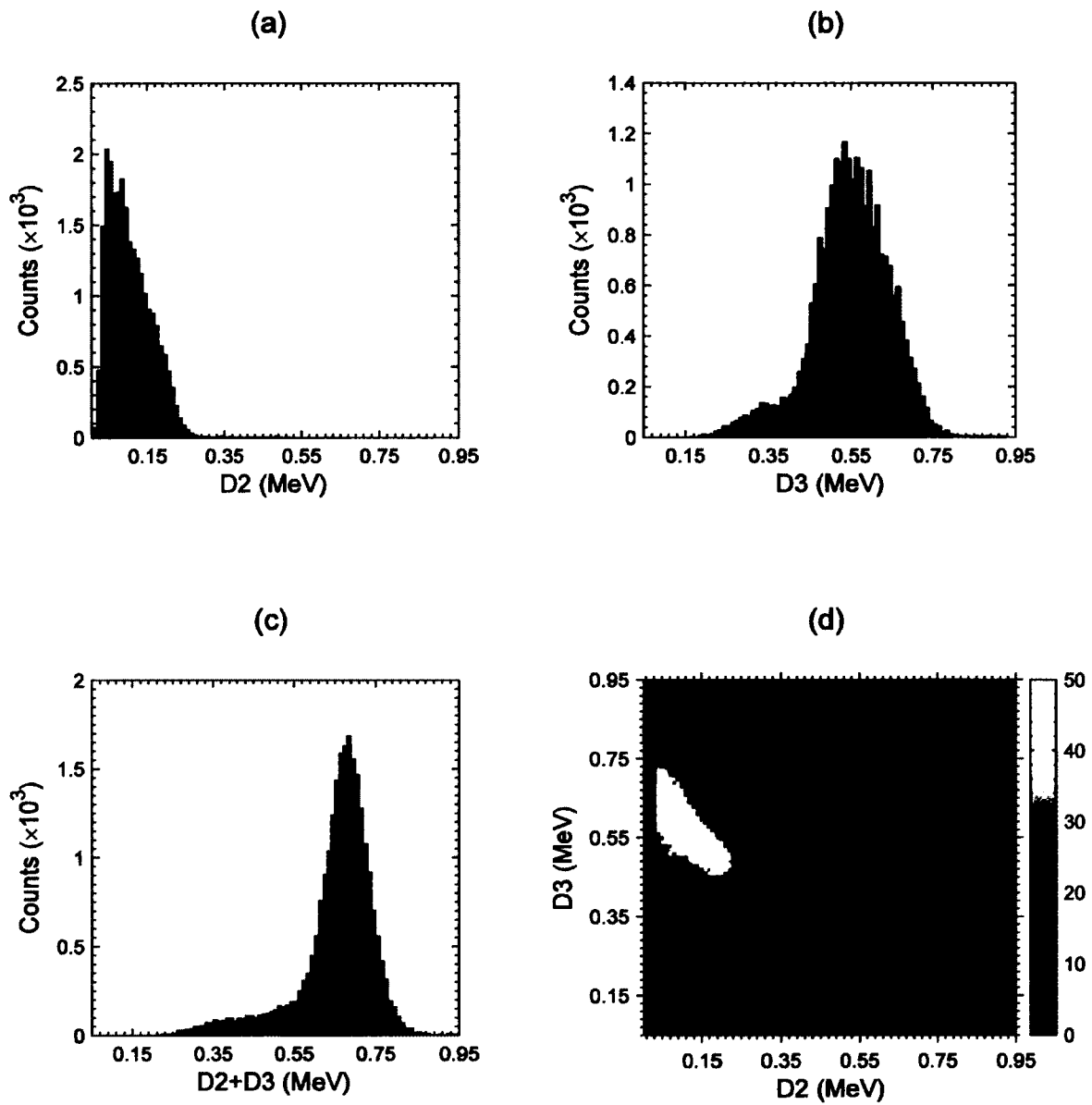


Figure A.8. Cs-137 D2-D3 coincidence data restricted to $\pm 5^\circ$ ARM measurements. Histograms of (a) D2 energy, (b) D3 energy, and (c) the net energy in D2 and D3. (d) A density plot of the D2 and D3 energies

The cause of these low-energy events cannot be attributed solely to background, electronic noise, or random coincidences because the count rate is greater than expected. The main cause of these events is γ -ray scattering off passive material into a cell. This would explain why the count rate below 0.2 MeV is greater for ^{60}Co calibration data compared to ^{137}Cs data. It also explains why the low-energy peak is more prominent for backscatters than forward scatters. The absence of this peak in the γ -ray measurements between D2 and D3 also supports this.

The large D3 cross section for γ -ray absorption should prevent most backscattering contributions to the low-energy peak. This is because γ rays that scatter off passive material into D3 will most likely be absorbed. These γ rays will not reach D2 or D2 and will therefore fail to meet coincidence requirements.

The coincidence requirement for the γ -ray detection layers is ten times less than that of the neutron detection layers. Scattering off passive material increases the ToF for γ rays. A smaller acceptance window for double-scatter coincidence should significantly reduce the number these events that are recorded. Also, due to the orientation of the scintillators (recall Figure 2.1), scattering off passive material into D2 are more likely to scatter from D2 towards D1 rather than D3.

A.4. Final Remarks

Analysis of the anomalous features in the D1 and D2 energy spectra below 0.2 MeV and above the Compton edge will be difficult because the exact nature of the interactions that occur cannot be determined. It has been shown that these features are easily eliminated with ToF and ARM cuts if these properties are known. All γ rays with energies less than 0.2 MeV were excluded in Section 2.7 because ARM calculations were

not possible with the ^{60}Co calibration data. Also, ToF cuts could not be made because the data were being used to characterize the NSPECT ToF system.

The results presented in this chapter support the conclusion that the majority of events creating the low-energy peak are caused by γ rays scattering off passive materials. This effect is essentially eliminated when the coincidence requirement is decreased from 50 ns to 5 ns and one organic scintillator is replaced with a scintillator that has a high γ -ray absorption cross section. Such modifications would, however, prevent D1 and D2 from detecting neutrons.

Additional testing is required to confirm the source of the low-energy peak. One possible approach is to place a γ -ray source, such as ^{133}Ba , on-axis and in front of NSPECT is recommended. Ba-133 is recommended because emitted γ rays have energies below 0.4 MeV. Scatters off passive material would leave these γ rays with energies too low for detection. The energy spectra from such a source should be devoid of any anomalous features below 0.2 MeV.